



On effective behavior of microstructures embedding general interfaces with damage

S. Saeb¹ · P. Steinmann^{1,2} · A. Javili³

Received: 16 August 2018 / Accepted: 15 May 2019 / Published online: 23 May 2019
© Springer-Verlag GmbH Germany, part of Springer Nature 2019

Abstract

The interface between constituents of a multiphase material exhibits properties different from those of the bulk and can lead to major alternation of the material response. Interface effects are particularly important for multiphase nano-materials where the area-to-volume ratio is significantly large. In this contribution, we study the influence of a degrading general interface. That is, we allow for the initiation and accumulation of damage on a generalized interface accounting for both jumps of the displacement and the traction across the interface. The applicability of the proposed framework is demonstrated through several numerical examples. We present a parametric study on the influence of a broad range of interface material parameters on the overall behavior of various microstructures subject to volumetric loading and unloading. The numerical results illustrate that the resistance *along* the interface plays a key role in the resulting damage mechanism and could potentially prevent the detachment of the inclusion from the matrix regardless of the resistance *across* the interface or bulk material parameters. This behavior is observed and shown for both two- and three-dimensional examples. Moreover, the size-effect due to the general interface model is examined and compared against other interface models. Finally, the influence of the boundary conditions on the effective response and damage initiation of several microstructures is studied.

Keywords Computational homogenization · Finite deformation · Elastic interface · Cohesive interface · General interface

1 Introduction

Almost all materials in nature are composed of different types of constituents and possess heterogeneous microstructures. The behavior of such materials is highly dependent on their composition at smaller scales and investigating their overall response requires detailed understanding of their underlying microstructures. Microstructures of materials are generally

different in material properties, volume fraction, shape and orientation of the constituents. Among these geometrical and physical complexities, the presence of interfaces between the constituents plays a key role since interfaces behave differently compared to the bulk. The influence of interfaces on the response of the materials becomes more noticeable as the size decreases due to a larger area-to-volume ratio. Therefore, interface effects are particularly significant for multiphase nano-materials where size effects are no longer negligible.

Understanding the behavior of materials accounting for surfaces and interfaces has been the subject of numerous studies [1–12]. The term “interface” refers to a zero-thickness model that represents the finite thickness “interphase” between different phases of a material. From this point of view, interfaces are two-dimensional manifolds in a three-dimensional space. Based on the jump conditions of various fields across the interface, several interface models can be defined. For mechanical problems, that are the focus of this manuscript, displacement and traction are the key fields to identify the interface type. The first family of interfaces is the *perfect interface model*. Choosing the term perfect stems from the fact that both the traction and the

✉ A. Javili
ajavili@bilkent.edu.tr

S. Saeb
saba.saeb@fau.de

P. Steinmann
paul.steinmann@fau.de

¹ Chair of Applied Mechanics, University of Erlangen–Nuremberg, Egerland Str. 5, 91058 Erlangen, Germany

² School of Engineering, University of Glasgow, Glasgow G12 8QQ, UK

³ Department of Mechanical Engineering, Bilkent University, 06800 Ankara, Turkey

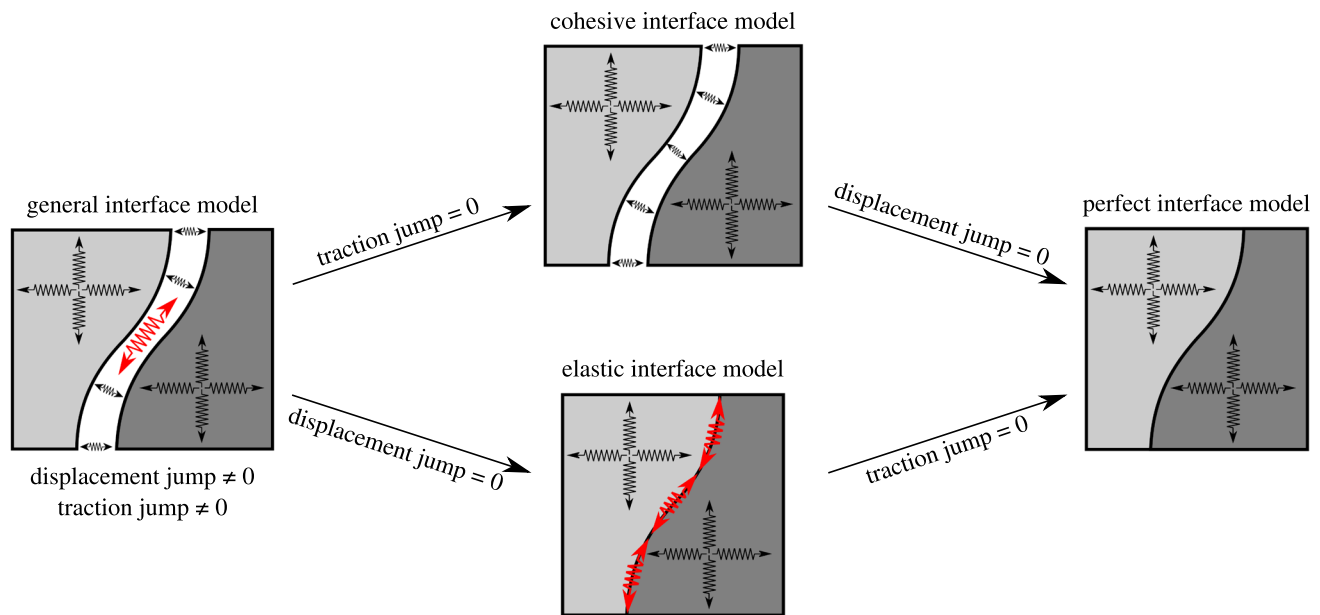


Fig. 1 Schematic clarification of different interface models. One limit of the above classification is the perfect interface model that does not allow for the displacement jump nor the traction jump across the inter-

face. The other limit corresponds to the general interface model which allows for both traction as well as displacement jump across the interface

displacement jumps across such an interface are continuous. This type of interface is the most widely used mainly due to its minor complexities from a computational point of view. Another well-known type of the interfaces is the *cohesive interface model* [13–16] which is particularly designed for modeling geometrically non-coherent structures as it allows for a displacement jump across the interface. However, traction continuity is a central assumption of this interface type [17]. The cohesive interface model has been utilized in a variety of applications such as modeling delamination and crack, and an extensive body of literature has been devoted to the development of this particular type of interface [18–29]. Another type of interfaces is the *elastic interface model* [30–34], which roots in the elastic surface model of Gurtin and Murdoch [35] that accounts for surfaces with their own constitutive behavior. The interface elasticity theory treats the interface essentially as a two-sided surface and it can thus be viewed as a generalization of the surface elasticity theory. In contrast to the cohesive interface model, the elastic interface model allows for the traction jump across the interface. The jump of the traction is associated with the resistance along the interface as well as the curvature of the interface. However, this model does not allow for a displacement jump and is only valid for geometrically coherent interfaces. Various aspects of the elastic interface model have been studied thoroughly in the literature from both analytical and computational points of view, see [36,37] among others. Clearly, both the cohesive and the elastic interface models are only two extremes of a *general interface model* allowing both jumps in the displacement and the traction field across the interface. Schematic

representations of different interface models are depicted in Fig. 1. In order to have a clear picture of the physical features of each interface model, in Fig. 2 we illustrate the effect of the interface models on deformation of two blocks with a zero-thickness interface model in between. The lower block is fixed at the bottom and the upper block is pulled from top. Both of the blocks are assumed to be elastic and have identical material properties. The perfect interface model perfectly bonds the blocks together as if the whole sample was one-piece. The cohesive interface model allows for opening of the interface and the upper block detaches from the lower one. The traction between the two blocks is a function of the opening and is obtained from traction-separation laws. The elastic interface model does not allow for an opening of the interface and thus the interface remains geometrically coherent. However, it results in a resistance along the interface against tangential stretches. Finally, the general interface is a combination of the cohesive and elastic interface models. In contrast to the cohesive and elastic interface models which are relatively well-established and well-understood, the general interface model remains somewhat ignored with the exceptions such as [38–41] which are mainly limited to analytical studies and small-strain problems. Only very recently, Javili et al. [42], Javili [43], Heitbreder et al. [44] presented some computational aspects of the general interface model in the context of the finite deformation setting. Moreover, general interface models in the context of thermal and thermo-mechanical problems have been discussed in [45,46], see also [47].

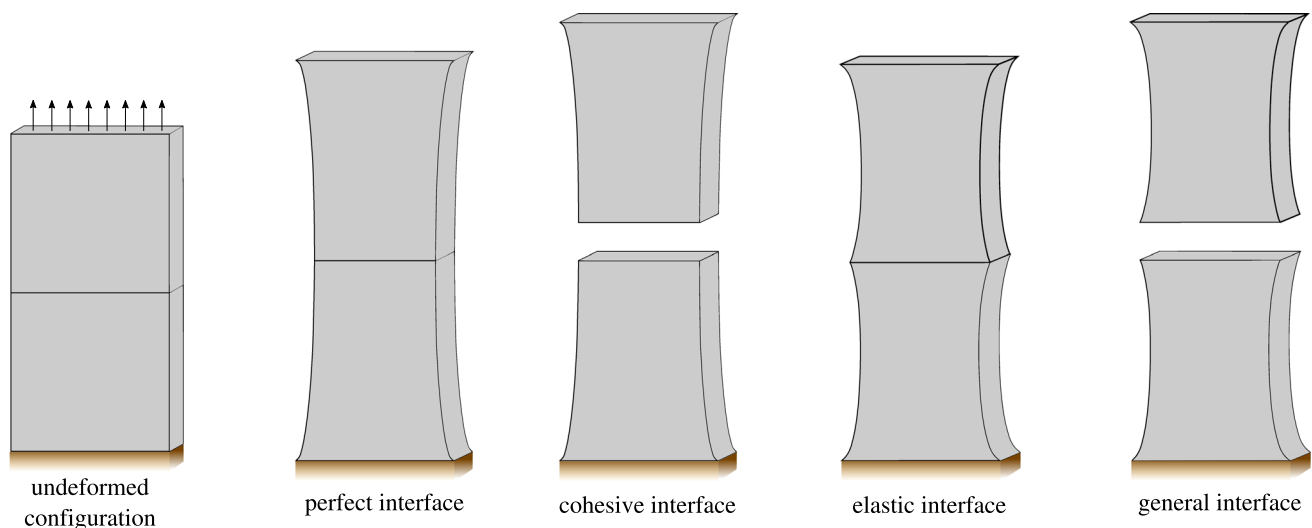


Fig. 2 Illustration of the effect of different interface models on deformation of two blocks with a zero-thickness interface model in between. The blocks are made of a same elastic material

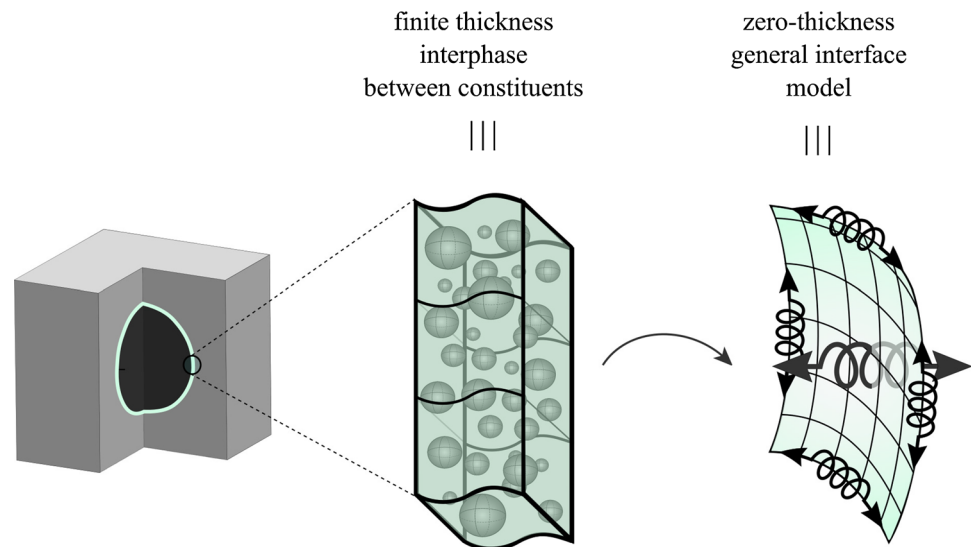
Predicting the behavior of a heterogeneous material is tightly linked to understanding the behavior of its microstructures. In order to model such materials [48–64], computational homogenization has been developed in the past. Detailed reviews can be found in [65–68]. The sample at the micro-scale is commonly referred to as the RVE (representative volume element). The boundary conditions to be imposed on the RVE are derived such that the equivalence of the virtual power between the scales is satisfied. Among the admissible boundary conditions, displacement (DBC), periodic (PBC) and traction (TBC) boundary conditions are canonical. The major limitation associated with the first-order micro-to-macro transition is lacking the ability to capture size effects, see [69,70] among others. A possible technique to overcome this shortcoming is to employ a second-order theory which requires the second gradient of the deformation [71,72]. An alternative methodology here is to account for the interfaces at the micro-scale. The influence of the cohesive and elastic interface model on the overall response of composites has been investigated for instance in [73–79]. However, incorporation of the general interface model is studied only very recently by Javili et al. [42]. They have shown that including general interfaces at the micro-scale results in complex and highly non-linear size effects which may be understood as combinations of smaller-stronger and smaller-weaker responses associated to the elastic and cohesive interface models, respectively. The interface behavior was however assumed to be elastic for simplicity and damage was not allowed on the interface which is not the case in the current contribution.

In fact, this work is mostly based on the framework developed in [42] and might be viewed as a complementary note on the results presented therein. In particular, Javili et

al. [42] assumed a hyperelastic behavior for the bulk and decomposed the response of the interface into tangential and orthogonal parts associated with resistance along and across the interface, respectively. The numerical results were, however, particularly designed for the case that the traction-separation law is linear elastic avoiding the degradation on the interface. One of the essential goals of this manuscript is to employ a more complicated model for the behavior of the material across the interface allowing for initiation and accumulation of damage across as well as along the interface while assuming a hyperelastic behavior for the bulk. Note that the key purpose of all the zero-thickness interfaces is to model a finite-thickness interphase between the constituents. The classical cohesive zone model only accounts for the resistance against the displacement jump on the interface and does not take the resistance against the stretching along the interface into account which is obviously a simplification of the interface behavior. Such simplification might lead to neglecting some crucial physical effects which arise from tangential resistance of the interface, see Fig. 3 and also the discussions in [80]. From this point of view, our proposed framework is an enhancement to the existing interface models and recovers the classical cohesive zone and elastic interface models only as its extremes. Therefore, we believe that the presented methodology is able to provide more accurate predictions for interfacial debonding.

The idea behind the present work is primarily motivated by the recently proposed micro-mechanical model of Dargazany and Itskov [81] to describe the *Mullins* effect in rubbers reinforced with fillers (silica or carbon black). The Mullins effect is commonly associated with the breakage of weak bonds between polymer chains and filler particles [82], the slippage of the polymer chains on the filler clusters [83] or the

Fig. 3 Schematic representation of a unit-cell embedded with a finite-thickness interphase between the constituents. We assume that a zero-thickness interface model can sufficiently replace the interphase region. The springs are assumed to undergo degradation here



damage of the polymer-filler network [84], see also [85–87]. Recently, Dargazany and Itskov [81] extended the previous works and proposed a novel micro-mechanical model that relates the Mullins effect to the loosening or breakage of the newly formed networks between the filler and the rubber. Generally, these bonds resist against the deformations in both *tangential* and *orthogonal* directions up to certain extent which is accompanied by initiation and accumulation of damage afterward. From a computational point of view, such a behavior can only be realized using a general interface model equipped with damage. Obviously, one could potentially allow also for damage and localization in the bulk at the micro-scale, and study the behavior of a macro-crack [88]. See [75,89,90] for additional examples of the materials in which interfacial debonding is the dominant mechanism. A similar problem to the one investigated here has only been studied very recently in [44] but only for two-dimensional unit-cell problem and for limited loading and boundary conditions. The key features of this manuscript compared to the previous studies in the literature are as follows.

- This contribution furnishes a comprehensive parametric study for a broad range of interface material parameters in order to clearly demonstrate the influence of each parameter on the effective response. The exhaustive set of results provide unprecedented information to better understand the behavior of heterogeneous materials when interfaces are present.
- In contrast to the previous studies on the subject often restricted to only loading condition, we study the behavior of microstructures under both volumetric loading and unloading conditions, which is computationally more challenging.
- Although the frameworks presented in the literature are reportedly suitable for large deformations of two- and

three-dimensional examples, the numerical results remain mostly limited to small-strain and two-dimensional problems. Here, for the first time, we demonstrate the generality of the framework through presenting the numerical simulations for both two- and three-dimensional examples with deformations of up to 200%.

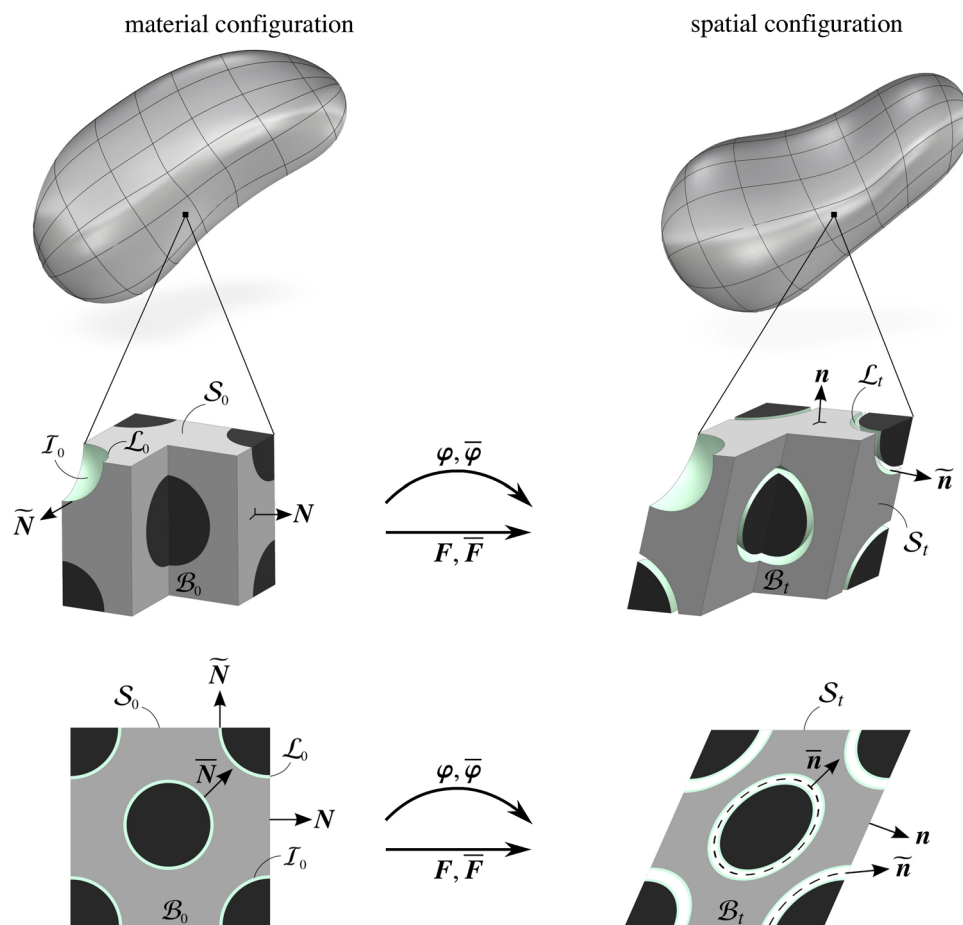
- To the best of our knowledge, the previous studies in the literature are limited to periodic boundary conditions (PBC) at the micro-scale. For the first time, we present a systematic comparison on the influence of the canonical boundary conditions on the overall response of several microstructures with random distribution of inclusions embedding general interfaces.

The remainder of this manuscript is organized as follows. The governing equations of the problem accounting for a general interface model are presented in Sect. 2. Section 3 details on the finite element formulation of the problem. The applicability of the presented framework is demonstrated through several numerical examples in Sect. 4. Finally, Sect. 5 concludes this work and provides further outlook.

2 Theory

The primary goal of this section is to elaborate on theoretical aspects of modeling large deformations of a unit-cell accounting for a general imperfect interface between the inclusion and the matrix. The constitutive response of the constituents are assumed to be known resulting in the unit-cell effective behavior. The input of the micro-problem is the macroscopic deformation gradient and the macroscopic Piola stress as the effective response is sought (Fig. 4).

Fig. 4 The material configuration \mathcal{B}_0 corresponds to a RVE which includes the geometrical information of the macroscopic point $^M\mathbf{X}$ mapped to its spatial configuration through the nonlinear deformation maps. The local macroscopic response is obtained through solving the associated boundary value problem at the micro-scale and averaging theorems



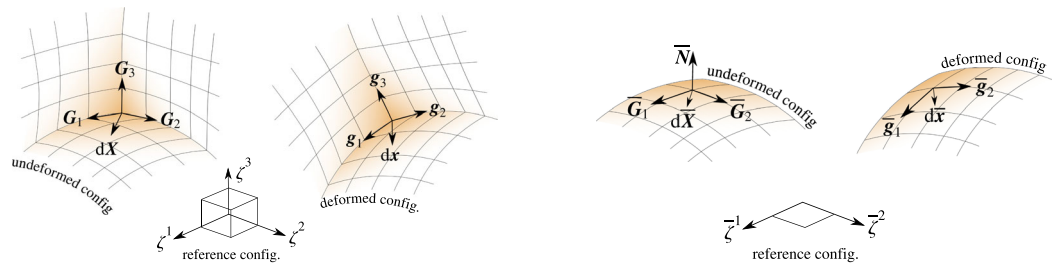
Let \mathcal{B}_0 and \mathcal{B}_t define the unit-cell in the material and spatial configuration, respectively. The material configuration consists of two disjoint subdomains, \mathcal{B}_0^+ and \mathcal{B}_0^- , intersecting at the interface \mathcal{I}_0 . The boundaries of \mathcal{B}_0^+ and \mathcal{B}_0^- are denoted $\partial\mathcal{B}_0^+$ and $\partial\mathcal{B}_0^-$, respectively. The boundary of the interface \mathcal{I}_0 is denoted \mathcal{L}_0 . Analogously, the interface and its boundary at the spatial configuration are denoted \mathcal{I}_t and \mathcal{L}_t , respectively. The external boundary of \mathcal{B}_0 is denoted \mathcal{S}_0 and does not include the interface \mathcal{I}_0 nor its boundary \mathcal{L}_0 . In a similar fashion, the external boundary of \mathcal{B}_t is denoted \mathcal{S}_t and does not contain the interface nor its boundary. The outward unit normals to \mathcal{S}_0 and \mathcal{S}_t are denoted \mathbf{N} and \mathbf{n} , respectively. The outward unit normals to \mathcal{L}_0 and \mathcal{L}_t are $\tilde{\mathbf{N}}$ and $\tilde{\mathbf{n}}$ and are tangent to \mathcal{I}_0 and \mathcal{I}_t . Note that $\tilde{\mathbf{N}}$ and $\tilde{\mathbf{n}}$ are not necessarily aligned with \mathbf{N} and \mathbf{n} . The unit normal to the interface \mathcal{I}_0 is denoted $\bar{\mathbf{N}}$ and is pointing from \mathcal{B}_0^- to \mathcal{B}_0^+ . Let \mathbf{X} define the placement of a point in \mathcal{B}_0 mapped to its spatial counterpart \mathbf{x} via $\mathbf{x} = \boldsymbol{\varphi}(\mathbf{X})$. In a similar fashion, we define the placement of a point on the interface \mathcal{I}_0 as $\bar{\mathbf{X}}$ mapped to its spatial counterpart $\bar{\mathbf{x}}$ on \mathcal{I}_t through $\bar{\mathbf{x}} = \bar{\boldsymbol{\varphi}}(\bar{\mathbf{X}})$. The bulk and the interface deformation gradients are defined as $\mathbf{F} = \text{Grad}\boldsymbol{\varphi}$ and $\bar{\mathbf{F}} = \overline{\text{Grad}}\bar{\boldsymbol{\varphi}} = \mathbf{F} \cdot \bar{\mathbf{I}}$, respectively, in which

the interface identity tensor (the projection tensor onto the interface) is defined by $\bar{\mathbf{I}} = \mathbf{I} - \bar{\mathbf{N}} \otimes \bar{\mathbf{N}}$. Therefore, the interface deformation gradient is a superficial tensor possessing the property $\bar{\mathbf{F}} \cdot \bar{\mathbf{N}} = \mathbf{0}$ and it is a rank-deficient tensor. Analogous to the bulk, the interface deformation gradient maps the interface material line element $d\bar{\mathbf{X}}$ to its counterpart in the spatial configuration $d\bar{\mathbf{x}}$ as $d\bar{\mathbf{x}} = \bar{\mathbf{F}} \cdot d\bar{\mathbf{X}}$ and it has, in general, nine components. Inverse mapping is clearly possible and reads $d\bar{\mathbf{X}} = \bar{\mathbf{f}} \cdot d\bar{\mathbf{x}}$ in which $\bar{\mathbf{f}}$ is the inverse of the interface deformation gradient and is connected to the interface identity tensor via the relation $\bar{\mathbf{f}} \cdot \bar{\mathbf{F}} = \bar{\mathbf{I}}$. Moreover, the determinant of $\bar{\mathbf{F}}$, denoted as $\overline{\text{Det}}\bar{\mathbf{F}}$, indicates the area change due to the interface deformation. Standard libraries do not provide adequate tools to evaluate the determinant and the inverse of a rank-deficient tensor. In the present work, we utilize the curvilinear coordinate system and employ the methodology proposed in [91] to evaluate the interface quantities. A summary of the formulations is given in Table 1.

The governing equations of the problem are the balances of linear and angular momentum. The balance of linear momentum in the bulk and on the interface reads

Table 1 Summary of some of the notations and definitions in the bulk and on the interface. The interface unit normal \bar{N} points from the minus to the plus side of the interface and can be computed as

$\bar{N} = \pm \bar{G}_1 \times \bar{G}_2 / |\bar{G}_1 \times \bar{G}_2|$. The \pm sign indicates that this formulation cannot determine the direction of the normal vector



Dimension	$3, \alpha = 1, 2, 3$	$2, \alpha = 1, 2$
Non-linear map	$\varphi(X)$	$\bar{\varphi}(\bar{X})$
Linear map	$dx = F \cdot dX$	$d\bar{x} = \bar{F} \cdot d\bar{X}$
Covariant bas.	$G_\alpha = dX/d\zeta^\alpha, g_\alpha = dx/d\zeta^\alpha$	$\bar{G}_\alpha = d\bar{X}/d\bar{\zeta}^\alpha, \bar{g}_\alpha = d\bar{x}/d\bar{\zeta}^\alpha$
Contravariant bas.	$G^\alpha = d\zeta^\alpha/dX, g^\alpha = d\zeta^\alpha/dx$	$\bar{G}^\alpha = d\bar{\zeta}^\alpha/d\bar{X}, \bar{g}^\alpha = d\bar{\zeta}^\alpha/d\bar{x}$
Identity tensor	$I = G_\alpha \otimes G^\alpha$	$\bar{I} = \bar{G}_\alpha \otimes \bar{G}^\alpha, \bar{i} = \bar{g}_\alpha \otimes \bar{g}^\alpha$
Gradient	$\text{Grad}\{\bullet\} = \partial\{\bullet\}/\partial\zeta^\alpha \otimes G^\alpha$	$\overline{\text{Grad}}\{\bullet\} = \partial\{\bullet\}/\partial\bar{\zeta}^\alpha \otimes \bar{G}^\alpha$
Divergence	$\text{Div}\{\bullet\} = \partial\{\bullet\}/\partial\zeta^\alpha \cdot G^\alpha$	$\overline{\text{Div}}\{\bullet\} = \partial\{\bullet\}/\partial\bar{\zeta}^\alpha \cdot \bar{G}^\alpha$
Def. grad.	$F = \frac{dx}{dX} = \frac{dx}{d\zeta} \cdot \frac{d\zeta}{dX} = \frac{dx}{d\zeta^\alpha} \otimes \frac{d\zeta^\alpha}{dX} = g_\alpha \otimes G^\alpha$	$\bar{F} = \frac{d\bar{x}}{d\bar{X}} = \frac{d\bar{x}}{d\bar{\zeta}} \cdot \frac{d\bar{\zeta}}{d\bar{X}} = \frac{d\bar{x}}{d\bar{\zeta}^\alpha} \otimes \frac{d\bar{\zeta}^\alpha}{d\bar{X}} = \bar{g}_\alpha \otimes \bar{G}^\alpha$
Def. grad. inv.	$f = \frac{dX}{dx} = \frac{dX}{d\zeta} \cdot \frac{d\zeta}{dx} = \frac{dX}{d\zeta^\alpha} \otimes \frac{d\zeta^\alpha}{dx} = G_\alpha \otimes g^\alpha$	$\bar{f} = \frac{d\bar{X}}{d\bar{x}} = \frac{d\bar{X}}{d\bar{\zeta}} \cdot \frac{d\bar{\zeta}}{d\bar{x}} = \frac{d\bar{X}}{d\bar{\zeta}^\alpha} \otimes \frac{d\bar{\zeta}^\alpha}{d\bar{x}} = \bar{G}_\alpha \otimes \bar{g}^\alpha$
Determinant	$\text{Det}\{\bullet\} = \frac{\{\bullet\} \cdot G_1 \cdot [\{\bullet\} \cdot G_2 \times \{\bullet\} \cdot G_3]}{G_1 \cdot [G_2 \times G_3]}$	$\overline{\text{Det}}\{\bullet\} = \frac{[\{\bullet\} \cdot \bar{G}_1 \times \{\bullet\} \cdot \bar{G}_2]}{\bar{G}_1 \cdot \bar{G}_2}$
Identity mat. rep.	$[I] = \begin{bmatrix} 1 & 0 & 0 \\ 0 & 1 & 0 \\ 0 & 0 & 1 \end{bmatrix}$	$[\bar{I}] = \begin{bmatrix} 1 & 0 & 0 \\ 0 & 1 & 0 \\ 0 & 0 & 0 \end{bmatrix}$
Def. grad. mat. rep.	$[F] = \begin{bmatrix} * & * & * \\ * & * & * \\ * & * & * \end{bmatrix}, [f] = \begin{bmatrix} * & * & * \\ * & * & * \\ * & * & * \end{bmatrix}$	$[\bar{F}] = \begin{bmatrix} * & * & 0 \\ * & * & 0 \\ * & * & 0 \end{bmatrix}, [\bar{f}] = \begin{bmatrix} * & * & * \\ * & * & * \\ 0 & 0 & 0 \end{bmatrix}$

$$\text{Div } P = 0 \quad \text{in } \mathcal{B}_0 \quad \text{subject to } P \cdot N = t_0 \quad \text{on } \mathcal{S}_0, \tag{1}$$

$$\overline{\text{Div}} \bar{P} + \llbracket P \rrbracket \cdot \bar{N} = 0 \quad \text{on } \mathcal{I}_0 \quad \text{subject to } \bar{P} \cdot \bar{N} = \bar{t}_0 \quad \text{on } \mathcal{L}_0, \tag{2}$$

respectively, where $\overline{\text{Div}} \bar{P} = \overline{\text{Grad}} \bar{P} : \bar{I}$ whereby the stresses in the bulk and on the interface are denoted by P and \bar{P} , respectively. Moreover, $\llbracket P \rrbracket \cdot \bar{N}$ represents the jump of the traction across the interface as $\llbracket P \rrbracket \cdot \bar{N} = [P^+ - P^-] \cdot \bar{N}$ where P^+ and P^- represent the Piola stresses in \mathcal{B}_0^+ and \mathcal{B}_0^- , respectively. Note, the interface Piola stress is a second order superficial tensor possessing the property $\bar{P} \cdot \bar{N} = 0$. The balance of angular momentum in the bulk and on the interface reads

$$\varepsilon : [F \cdot P^t] = 0, \quad [x] \times \llbracket P \rrbracket \cdot \bar{N} + \varepsilon : [\bar{F} \cdot \bar{P}^t] = 0, \tag{3}$$

respectively, where ε is the third-order permutation tensor and the average operator is defined by $\llbracket \{\bullet\} \rrbracket = \frac{1}{2}[\{\bullet\}^+ + \{\bullet\}^-]$. It is of crucial importance to note that the format of the balance of angular momentum given in (3)₂ is derived assuming that the motion of the interface is dependent on the bulk and $\bar{x} = \{\{x\}\}$. Neglecting this assumption leads to a more complicated format of the balance of angular momentum on the interface discussed in [42].

In the presence of general interfaces, the classical definition for the effective response does not necessarily hold. Following the extended averaging theorems, the effective response accounting for general interfaces as a response to an effective deformation ${}^M F$ is defined as

$$\begin{aligned} {}^M P &= \frac{1}{\mathcal{V}_0} \int_{\mathcal{B}_0} P \, dV + \frac{1}{\mathcal{V}_0} \int_{\mathcal{I}_0} \bar{P} \, dA \\ &= \frac{1}{\mathcal{V}_0} \int_{\mathcal{S}_0} t_0 \otimes X \, dA + \frac{1}{\mathcal{V}_0} \int_{\mathcal{L}_0} \bar{t}_0 \otimes \bar{X} \, dL, \end{aligned} \tag{4}$$

in which \mathcal{V}_0 is the total volume of the RVE. Clearly, the definition of the effective response depends, in addition to the bulk, on the elastic response along the interface. In the absence of interface effects, the classical definition of effective response is recovered. Moreover, the micro-scale incremental energy is extended by two contributions from the response along and across the interface and the extended Hill–Mandel condition reads

$$\underbrace{\frac{1}{\mathcal{V}_0} \int_{\mathcal{B}_0} \mathbf{P} : \delta \mathbf{F} \, dV}_{\text{bulk}} + \underbrace{\frac{1}{\mathcal{V}_0} \int_{I_0} \bar{\mathbf{P}} : \delta \bar{\mathbf{F}} \, dA}_{\text{along the interface}} + \underbrace{\frac{1}{\mathcal{V}_0} \int_{I_0} \{\{ \mathbf{t} \} \} \cdot [\![\delta \boldsymbol{\varphi}]\!] \, dA}_{\text{across the interface}} - \underbrace{\mathbf{M} \mathbf{P} : \delta^M \mathbf{F}}_{\text{macro-scale}} \doteq 0. \tag{5}$$

Finally, we prescribe the canonical boundary conditions on the micro-problem.

3 Computational aspects

This section presents the details of the finite element formulation of the micro-scale problem accounting for general imperfect interfaces. First, the weak form of the balance of linear momentum is derived. Next, the weak form is discretized in space. Finally, the resulting nonlinear system of equations is linearized and solved using appropriate schemes.

In order to obtain the weak form of the balance of linear momentum, the left hand side of Eqs. (1) and (2) are tested with vector valued test functions, $\delta \boldsymbol{\varphi}$ and $\delta \bar{\boldsymbol{\varphi}}$, respectively and are integrated over the bulk and interface domain in the material configuration. Through combining the resulting equations and employing the bulk and the interface divergence theorems along with considering the superficiality of the interface Piola stress and the assumption that $\delta \bar{\boldsymbol{\varphi}} = \{\{ \delta \boldsymbol{\varphi} \} \}$, we obtain the weak form of the balance of linear momentum as

$$\int_{\mathcal{B}_0} \mathbf{P} : \text{Grad} \delta \boldsymbol{\varphi} \, dV - \int_{S_{0,N}} \delta \boldsymbol{\varphi} \cdot \mathbf{t}_0 \, dA + \int_{I_0} \bar{\mathbf{P}} : \overline{\text{Grad} \delta \bar{\boldsymbol{\varphi}}} \, dA + \int_{I_0} \{\{ \mathbf{t} \} \} \cdot [\![\delta \boldsymbol{\varphi}]\!] \, dA \doteq 0 \quad \forall \delta \boldsymbol{\varphi} \in \mathcal{H}_0^1(\mathcal{B}_0), \tag{6}$$

where $S_{0,N}$ refers to the Neumann portion of the (bulk) boundary. Next, the material domain is discretized into sets of bulk, surface and interface finite elements as

$$\mathbf{A}_{\beta=1}^{\#be} \int_{\mathcal{B}_0^\beta} \mathbf{P} : \text{Grad} \delta \boldsymbol{\varphi} \, dV - \mathbf{A}_{\gamma=1}^{\#se} \int_{S_{0,N}^\gamma} \delta \boldsymbol{\varphi} \cdot \mathbf{t}_0 \, dA + \mathbf{A}_{\alpha=1}^{\#ie} \int_{I_0^{\alpha+}} \frac{1}{2} \bar{\mathbf{P}} : \overline{\text{Grad} \delta \bar{\boldsymbol{\varphi}}} \, dA$$

$$+ \mathbf{A}_{\alpha=1}^{\#ie} \int_{I_0^{\alpha-}} \frac{1}{2} \bar{\mathbf{P}} : \overline{\text{Grad} \delta \bar{\boldsymbol{\varphi}}} \, dA + \mathbf{A}_{\alpha=1}^{\#ie} \int_{I_0^{\alpha+}} \{\{ \mathbf{t} \} \} \cdot \delta \bar{\boldsymbol{\varphi}} \, dA - \mathbf{A}_{\alpha=1}^{\#ie} \int_{I_0^{\alpha-}} \{\{ \mathbf{t} \} \} \cdot \delta \bar{\boldsymbol{\varphi}} \, dA \doteq 0, \tag{7}$$

where #be, #se and #ie represent the number of bulk, surface and interface elements, respectively. The domain of the

bulk element β is denoted \mathcal{B}_0^β . The domain of the surface element γ upon which traction is prescribed is denoted $S_{0,N}^\gamma$. The interface element α on the plus and minus sides of the interface is denoted $I_0^{\alpha+}$ and $I_0^{\alpha-}$, respectively. The fully discretized weak form of the balance of linear momentum is obtained by replacing the test functions with their spatial Bubnov–Galerkin approximations together with the isoparametric concept as

$$\mathbf{R}^I := \mathbf{A}_{\beta=1}^{\#be} \int_{\mathcal{B}_0^\beta} \mathbf{P} \cdot \text{Grad} N^i \, dV - \mathbf{A}_{\gamma=1}^{\#se} \int_{S_{0,N}^\gamma} \delta \boldsymbol{\varphi} \cdot \mathbf{t}_0 \, dA + \mathbf{A}_{\alpha=1}^{\#ie} \int_{I_0^{\alpha+}} \frac{1}{2} \bar{\mathbf{P}} \cdot \overline{\text{Grad} \bar{N}^i} \, dA + \mathbf{A}_{\alpha=1}^{\#ie} \int_{I_0^{\alpha-}} \frac{1}{2} \bar{\mathbf{P}} \cdot \overline{\text{Grad} \bar{N}^i} \, dA + \mathbf{A}_{\alpha=1}^{\#ie} \int_{I_0^{\alpha+}} \{\{ \mathbf{t} \} \} \cdot \bar{N}^i \, dA - \mathbf{A}_{\alpha=1}^{\#ie} \int_{I_0^{\alpha-}} \{\{ \mathbf{t} \} \} \cdot \bar{N}^i \, dA \doteq \mathbf{0}. \tag{8}$$

The fully discretized form of the residual associated with the global node I is denoted by the vector \mathbf{R}^I in which i represents the local node of a finite element corresponding to the global node I . The shape functions in the bulk and on the interface associated with the local node i are denoted N^i and \bar{N}^i . The nodal residuals are then collected into a global residual vector \mathbf{R} as

$$\mathbf{R} = \mathbf{R}(\mathbf{d}) \doteq \mathbf{0} \quad \text{with} \quad \mathbf{R} = [\mathbf{R}^1 \dots \mathbf{R}^I \dots \mathbf{R}^{\#n}]^t, \tag{9}$$

in which \mathbf{d} denotes the unknown global vector of displacements and #n denotes the number of nodes. In order to solve the non-linear system (9), the Newton–Raphson method can be employed. However, this method may lead to numerical instabilities when softening behavior appears in the material response. In this contribution, as will be discussed in

following sections, we allow for initiation and accumulation of damage on the interface leading to gradual or sudden abrupt in the resistance across and along the interface. This, in turn, can lead to softening in the overall behavior of the material. In order to capture such behavior, the arc-length method [92,93] is implemented and utilized to run the numerical examples. For instance, when we impose DBC to solve the micro-problem, we satisfy this boundary condition using the penalty method and impose it as a constraint to the non-linear system (9) as

$$\mathbf{R}(\mathbf{d}) + \Pi \mathbf{E} [\mathbf{d} - \lambda \mathbf{d}^*] \doteq \mathbf{0}, \quad (10)$$

where Π is the penalty parameter and has to be chosen sufficiently large, \mathbf{E} is the diagonal matrix containing ones on the boundary nodes where \mathbf{d}^* is prescribed with \mathbf{d}^* being the global vector of prescribed displacements. The linearization of the non-linear system (10) is given in [94] and is not presented here for the sake of space. The implementation of PBC follows nearly the the same methodology with the difference that, for instance for a rectangular unit-cell, the deformations of the corner nodes are prescribed through the constraint in the penalty method and the displacements of the remaining boundary nodes are evaluated assuming that the fluctuations are periodic. Implementation of TBC, on the other hand, fits perfectly to the arc-length method in its original format (force driven) but requires introduction of a new Lagrange multiplier to satisfy uniform distribution of traction on the boundary. Another alternative methodology to implement TBC is to employ semi-Dirichlet boundary condition [95].

4 Numerical examples

The main goal of this section is to illustrate the performance of the presented scheme via a series of numerical examples and to investigate the effect of the general interface model on the response of the microstructure. In order to proceed, we specify free energies for both the bulk and the interface and consequently derive the constitutive laws. For the bulk at the micro-scale, we assume a hyperelastic neo-Hookean energy density per unit volume in the material configuration

$$\psi(\mathbf{F}) = \frac{1}{2} \mu [\mathbf{F} : \mathbf{F} - 3 - 2 \log J] + \frac{1}{2} \lambda \log^2 J \quad \text{with} \quad J = \text{Det} \mathbf{F}, \quad (11)$$

in which μ and λ denote the bulk Lamé parameters.

For the material behavior of the interface, we additively split the interface free energy density $\bar{\psi}$ into a tangential part associated to elastic interface model and an orthogonal part associated to cohesive interface model, as

$$\bar{\psi}(\bar{\mathbf{F}}, \llbracket \boldsymbol{\varphi} \rrbracket) = \bar{\psi}_{\parallel}(\bar{\mathbf{F}}) + \bar{\psi}_{\perp}(\llbracket \boldsymbol{\varphi} \rrbracket). \quad (12)$$

For the material response along the the interface, we assume a hyperelastic neo-Hookean energy density per unit area in the material configuration

$$\bar{\psi}_{\parallel}(\bar{\mathbf{F}}) = \frac{1}{2} \bar{\mu} [\bar{\mathbf{F}} : \bar{\mathbf{F}} - 2 - 2 \log \bar{J}] + \frac{1}{2} \bar{\lambda} \log^2 \bar{J} \quad \text{with} \quad \bar{J} = \text{Det} \bar{\mathbf{F}}, \quad (13)$$

where $\bar{\mu}$ and $\bar{\lambda}$ are the interface material parameters, see [91]. In a two-dimensional structure, the interface is a one-dimensional manifold which, along the interface, resists only against its length change. In this case, it is sufficient to introduce only one material parameter to define the elastic behavior along the interface. The material response across the interface is assumed to be governed by a classical cohesive energy taking the form

$$\bar{\psi}_{\perp}(\llbracket \boldsymbol{\varphi} \rrbracket) = \exp(1) \sigma_c \delta_c \left[1 - \left[1 + \frac{\llbracket \boldsymbol{\varphi} \rrbracket}{\delta_c} \right] \exp\left(\frac{-\llbracket \boldsymbol{\varphi} \rrbracket}{\delta_c}\right) \right], \quad (14)$$

in which δ_c and σ_c are parameters that govern the cohesive behavior. According to this definition, for displacement jumps smaller that δ_c , the traction across the interface rises as the displacement jump across the interface increases. However, as soon as the opening across the interface reaches δ_c , the traction decreases exponentially leading to accumulation of substantial damage in the material, see Fig. 5. As a measure of damage at each point on the interface, we define a damage parameter \mathcal{D} which is calculated as [16]

$$\mathcal{D} = \frac{\bar{\psi}_{\perp}(\llbracket \boldsymbol{\varphi} \rrbracket_{\max})}{\bar{\psi}_{\perp}(\infty)} = \frac{\bar{\psi}_{\perp}(\llbracket \boldsymbol{\varphi} \rrbracket_{\max})}{\exp(1) \sigma_c \delta_c} \quad \text{with} \quad \dot{\mathcal{D}} \geq 0, \quad (15)$$

where $\llbracket \boldsymbol{\varphi} \rrbracket_{\max}$ is the maximum attained displacement. Damage parameter \mathcal{D} ranges from 0 to 1 with 0 representing no damage and 1 indicating complete decohesion of the interface.

Another assumption that we make in the current framework is that when damage occurs across the interface, it influences the behavior along the interface similarly as

$$\bar{\psi}_{\parallel}(\bar{\mathbf{F}}) = [1 - \mathcal{D}] \left[\frac{1}{2} \bar{\mu} [\bar{\mathbf{F}} : \bar{\mathbf{F}} - 2 - 2 \log \bar{J}] + \frac{1}{2} \bar{\lambda} \log^2 \bar{J} \right]. \quad (16)$$

Therefore, when $\mathcal{D} = 0$, the resistance against and along the interface is intact and for $\mathcal{D} = 1$, the interface effects fully vanish. Next, the Clausius–Duhem inequality is used to derive associated bulk and interface Piola stress tensors and traction-separation law as

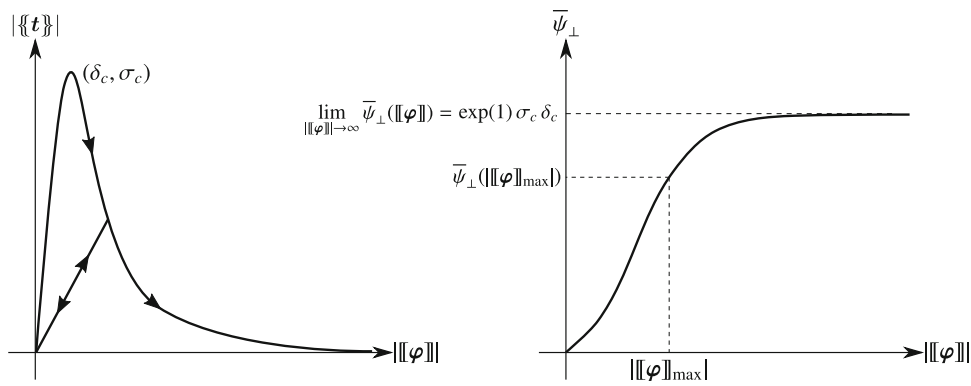


Fig. 5 (left) Exponential relation for traction-separation law under loading condition and linear relation assumption between displacement and traction when sample is unloaded. (right) Damage parameter \mathcal{D} is evaluated locally at each point on the interface and is the ratio of current

attained energy across the interface over the strain energy release rate (fracture energy). Therefore, $\mathcal{D} = 1$ when full decohesion takes place and $\mathcal{D} = 0$ when interface is completely closed

$$\begin{aligned} \mathbf{P} &= \frac{\partial \psi}{\partial \mathbf{F}} = \mu[\mathbf{F} - \mathbf{F}^{-t}] + \lambda \log J \mathbf{F}^{-t}, \\ \bar{\mathbf{P}} &= \frac{\partial \bar{\psi}_\parallel}{\partial \bar{\mathbf{F}}} = [1 - \mathcal{D}] \left[\bar{\mu}[\bar{\mathbf{F}} - \bar{\mathbf{F}}^{-t}] + \bar{\lambda} \log \bar{J} \bar{\mathbf{F}}^{-t} \right], \\ \{\{t\}\} &= \frac{\partial \bar{\psi}_\perp}{\partial \|\{\varphi\}\|} = \exp(1) \sigma_c \frac{1}{\delta_c} \exp\left(\frac{-\|\{\varphi\}\|}{\delta_c}\right) \|\{\varphi\}\|. \end{aligned} \tag{17}$$

$$\begin{aligned} \bar{\mathbb{A}}_\perp &= \frac{\partial^2 \bar{\psi}_\perp}{\partial \|\{\varphi\}\|^2} = \exp(1) \sigma_c \frac{1}{\delta_c} \exp\left(\frac{-\|\{\varphi\}\|}{\delta_c}\right) \mathbf{I} \\ &\quad - \exp(1) \frac{\sigma_c}{\delta_c^2} \frac{1}{\|\{\varphi\}\|} \exp\left(\frac{-\|\{\varphi\}\|}{\delta_c}\right) \|\{\varphi\}\| \otimes \|\{\varphi\}\|. \end{aligned} \tag{19}$$

Note that (14) and (17)₃ hold only under loading condition. In the case of unloading, it is assumed that the traction-separation law takes the form

Two nonstandard tensor products $\bar{\otimes}$ and $\underline{\otimes}$ of two second-order tensors \mathbf{A} and \mathbf{B} are the fourth-order tensors $\mathbb{D} = \mathbf{A} \bar{\otimes} \mathbf{B}$ with $D_{ijkl} = A_{ik} B_{jl}$ and $\mathbb{C} = \mathbf{A} \underline{\otimes} \mathbf{B}$ with $C_{ijkl} = A_{il} B_{jk}$.

$$\{\{t\}\} = \frac{\|\{\{t\}\}_{\max}\|}{\|\{\varphi\}\|_{\max}} \|\{\varphi\}\|, \tag{18}$$

The computational studies are conducted mostly on the unit-cells showcased in Fig. 6 and the deformation type for all the numerical studies is a volumetric expansion.

where $\|\{\{t\}\}_{\max}\|$ is the traction vector evaluated at $\|\{\varphi\}\|_{\max}$ using (17)₃.

Remark 1 A volumetric expansion is chosen mainly due to the fact that it leads to a more pronounced change in the interface area as compared to other deformation types such as simple shear deformation, see Fig. 7. This, in turn, leads to a more significant interface effect on the overall response which is the main focus of the current study. Note that the interface model here does not possess a flexural resistance and is hence insensitive to bending. In addition, numerical examples under a shear deformation involves contact mechanics and introduces more complications without providing any additional insight.

In order to solve the system of Eq.(9), in addition to the Piola stresses, the bulk Piola tangent \mathbb{A} and the interface Piola tangents $\bar{\mathbb{A}}_\parallel$ and $\bar{\mathbb{A}}_\perp$ are required and calculated as

$$\begin{aligned} \mathbb{A} &= \frac{\partial^2 \psi}{\partial \mathbf{F}^2} = \mu [\mathbf{I} \bar{\otimes} \mathbf{I} + \mathbf{F}^{-t} \underline{\otimes} \mathbf{F}^{-1}] \\ &\quad + \lambda [\mathbf{F}^{-t} \otimes \mathbf{F}^{-t} - \log J \mathbf{F}^{-t} \underline{\otimes} \mathbf{F}^{-1}], \\ \bar{\mathbb{A}}_\parallel &= \frac{\partial^2 \bar{\psi}_\parallel}{\partial \bar{\mathbf{F}}^2} = [1 - \mathcal{D}] \bar{\mu} \left[\mathbf{I} \bar{\otimes} \bar{\mathbf{I}} + \bar{\mathbf{F}}^{-t} \underline{\otimes} \bar{\mathbf{F}}^{-1} \right. \\ &\quad \left. - [\bar{\mathbf{F}} \cdot \bar{\mathbf{F}}^{-1}] \bar{\otimes} [\bar{\mathbf{F}}^{-1} \cdot \bar{\mathbf{F}}^{-1}] \right] \\ &\quad + [1 - \mathcal{D}] \bar{\lambda} \left[\bar{\mathbf{F}}^{-t} \otimes \bar{\mathbf{F}}^{-t} - \log \bar{J} [\bar{\mathbf{F}}^{-t} \underline{\otimes} \bar{\mathbf{F}}^{-1} \right. \\ &\quad \left. - [\bar{\mathbf{F}} \cdot \bar{\mathbf{F}}^{-1}] \bar{\otimes} [\bar{\mathbf{F}}^{-1} \cdot \bar{\mathbf{F}}^{-1}] \right], \end{aligned}$$

Remark 2 Obviously, the circular microstructure shown in Fig. 6 is not a representative cut-out volume of a real microstructure. However, it can be shown that the effective bulk modulus obtained from the circular unit-cell coincides with the one from different boundary conditions applied to rectangular microstructures as the number of inclusions increases [96], see Fig. 8. This observation has been the primary motivation to perform numerical studies on a simplified circular unit-cell in the present work. Moreover, the choice of a circular unit-cell under volumetric expansion loading results in a symmetric overall response and allows

Fig. 6 Three types of unit-cells are employed to conduct the numerical simulations. The two- and three-dimensional unit-cells are discretized using four- and eight-node bilinear bulk and linear and four-node bilinear interface elements, respectively. For all the numerical simulations, volumetric expansion is imposed on the boundary of the unit-cells via the macroscopic deformation gradient

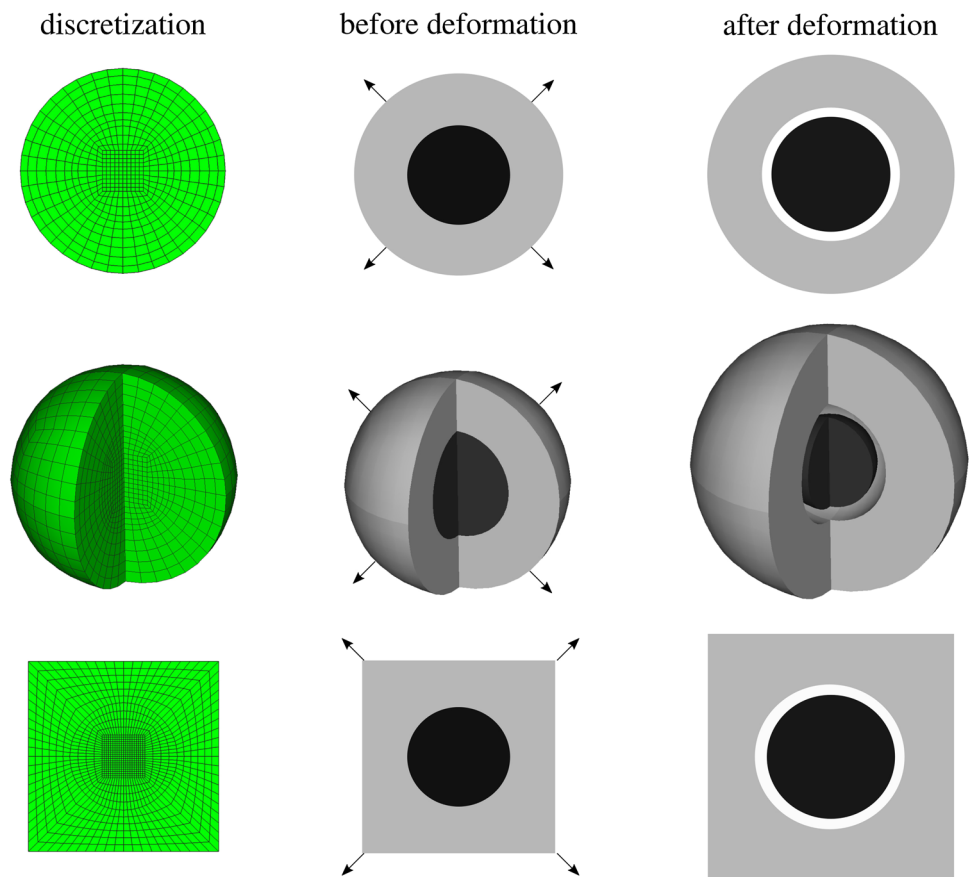
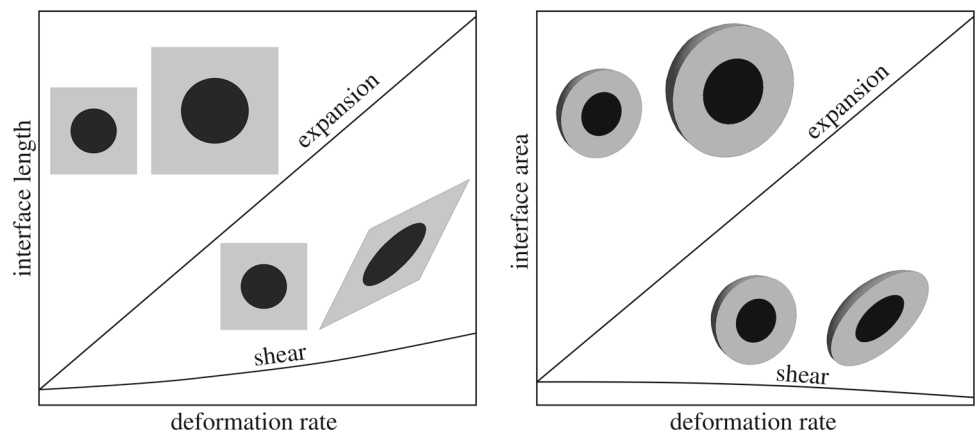


Fig. 7 Volumetric expansion yields more significant length/area change of the interface than the shear deformation



for better interpretation of the results. A rectangular unit-cell is employed only in the last section where the influence of different boundary conditions on the overall response is examined.

The effective property of interest in this contribution is the xx -component of the macroscopic Piola stress, however, other alternatives and valid choices qualitatively lead to the same trends and conclusions. We discretize the unit-cells using linear bulk and interface elements in both two and three dimensions. The main advantage of having the same polynomial order for bulk and interface elements is that the facets

of two adjacent bulk elements can be regarded as the two sides of an interface element and therefore we do not require further interpolations or hanging nodes to properly connect the interface to its surrounding bulk. All the numerical examples are solved using our in-house finite element code. The numerical examples are devised such that they cover various aspects of the theory for a broad range of parameters and various loading and boundary conditions.

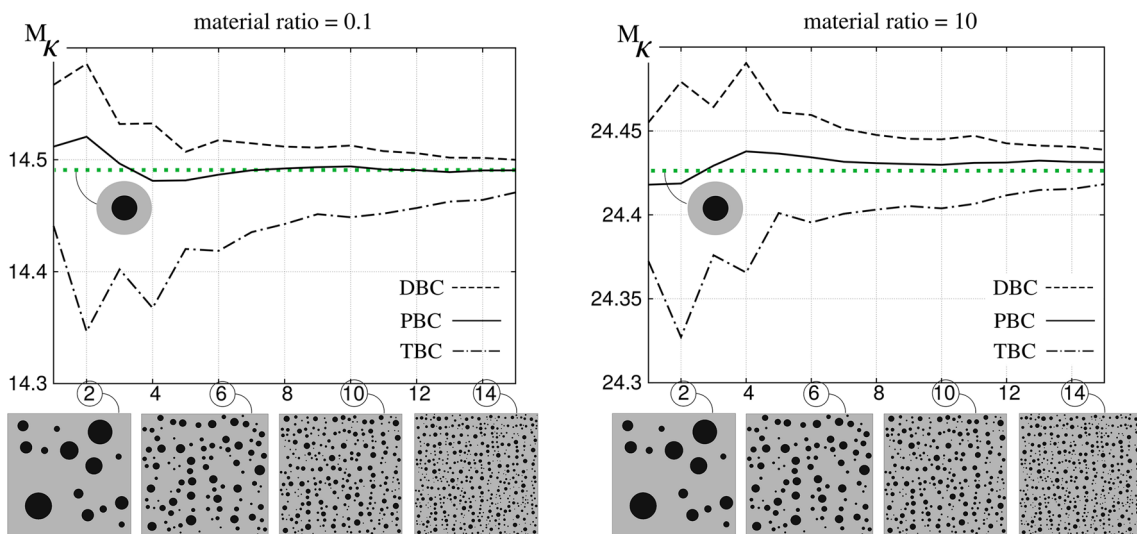


Fig. 8 The effective bulk modulus obtained from the circular unit-cell coincides with the effective value obtained from the convergence of different boundary conditions as the number of inclusions within the microstructure increases

4.1 Parametric study

This section presents a parametric study on the influence of the interface material parameters $(\bar{\mu}, \delta_c, \sigma_c)$ on the overall response of the circular unit-cell when it undergoes 100% of volumetric expansion deformation. The inclusion is assumed to be 10 times stiffer than the matrix. Figure 9 shows the change in effective response and the damage parameter \mathcal{D} calculated on the interface with respect to different values of $\delta_c \in [0.1, 10]$ and $\sigma_c \in [0.1, 100]$. Note that the geometry of the unit-cell as well as the loading type (volumetric expansion) are symmetric. Therefore, \mathcal{D} is equal for all the points on the interface. Different surfaces in the figures represent the results for various values of $\bar{\mu} = 0, 40, 1000$. For comparison purposes, we also include the effective response of a unit-cell with a circular void at its center (with no interface or surface effect) represented here by solid surface in Fig. 9.

First, $\bar{\mu}$ is set to 0. Doing so results in simplifying the general interface model to the cohesive interface model. The numerical results indicate that when δ_c and σ_c are set to small values, \mathcal{D} gets close to 1 indicating decohesion of the inclusion from the matrix. This is mainly due to two reasons. First, The traction between the constituents is so small and does not resist against the displacement jump across the interface and second, the critical displacement jump is small and is exceeded as soon as a small deformation is applied on the boundary leading to further reduction in the traction across the interface. Clearly, when the inclusion is fully detached from the matrix, the overall response of the unit-cell would coincide with the one obtained for a unit-cell with a circular void at its center. The results confirm that by increasing σ_c and keeping δ_c small, the traction across the interface becomes large enough to keep the inclusion next to the matrix resulting

in smaller \mathcal{D} . When δ_c is set to larger values, for small values of σ_c , the overall response mostly coincides with the effective response of a unit-cell with a void although \mathcal{D} remains relatively small. This is due to the fact that larger δ_c along with small values of σ_c allow for larger opening across the interface without accumulation of damage and softer overall response of the interface. In other words, for this set of parameters, the traction-separation law becomes almost linear for moderate loading cases with the traction increasing at a minor rate with respect to the displacement jump. Obviously, increasing σ_c while keeping δ_c large leads to stiffer overall responses and further reduction in \mathcal{D} .

Next, $\bar{\mu}$ is set to 40. Setting a non-zero value for $\bar{\mu}$ induces an additional resistance along the interface. Numerical results show that in this case the effective responses deviate from the ones obtained for $\bar{\mu} = 0$ specifically when \mathcal{D} is not large. This is justified by the fact that when \mathcal{D} is large, the resistance along the interface weakens as well. On the other hand, for small values of \mathcal{D} , the elastic interface contributes to the effective response leading to a larger overall response.

Finally, $\bar{\mu}$ is set to a considerably large value of 1000. Under such condition, the elasticity along the interface becomes the dominant mechanism of the micro-structure leading to substantial resistance against the deformations along the interface. As a result, it enables the interface to keep the inclusion and the matrix close to each other for all values of σ_c and δ_c and avoids accumulation of damage on the interface. Obviously, the damage parameter \mathcal{D} remains almost constant and close to zero for all cohesive interface material parameters. Note that the effective response obtained in this case coincides with the one obtained for the previous cases when σ_c and δ_c are set to large and small values, respectively. Therefore, we conclude that increasing the elastic interface

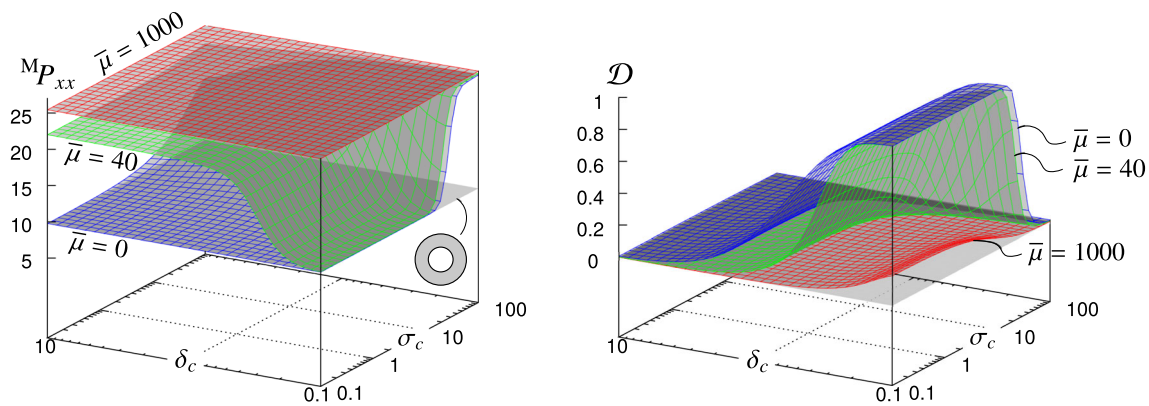


Fig. 9 xx -component of the macroscopic Piola stress (left) and damage parameter (right) with varying δ_c and σ_c when the inclusion is 10 times stiffer than the matrix. Different surfaces represent the results for

different values of elastic interface material parameter $\bar{\mu}$. The grey surface indicates the results for a unit-cell with a void at its center whose boundary is assumed to be non-energetic

material parameter resembles stiffening of the material across the interface. It is worth mentioning that although the lower bound of the effective responses in Fig. 9 coincides with the one from the unit-cell with a circular void, the effective response obtained from a unit-cell with a rigid inclusion may not necessarily cover the upper bound of the effective response, due to the damage.

Note that when $\bar{\mu} = 0$ (cohesive interface) and σ_c is very large, the inclusion and the matrix are kept firmly close to each other due to the large traction between them. The overall response obtained under such conditions is the stiffest attainable response given that $\bar{\mu}$ is zero. In this case, the cohesive interface model imitates the perfect interface model. However, increasing $\bar{\mu}$ leads to additional stresses and a stiffer overall response compared to the cohesive interface model. This behavior may not be observed easily in Fig. 9 mainly due to the fact that the inclusion is assumed to be 10 times stiffer than the matrix which limits the contribution of the elastic interface on the overall response. In order to highlight the elastic interface effect, the same study is conducted when the inclusion and the matrix are identical, see Fig. 10. Clearly, under such conditions there is a considerable gap between the results of the general interface and the stiffest attainable response from the cohesive interface.

4.2 Loading and unloading

Next, we study the change in overall response of the circular unit-cell when it undergoes 150% of volumetric expansion through three loading and unloading stages. The inclusion is assumed to be 10 times stiffer than the matrix. This set of numerical examples is carried out for different values for the elastic interface material parameters $\bar{\mu}$ while the cohesive interface material parameters are fixed to $\sigma_c = 10$ and $\delta_c = 0.12$. The solid lines and the dashed lines in the fig-

ures represent the loading phase and the unloading phase, respectively.

Numerical results in Fig. 11 confirm that when $\bar{\mu}$ is set to 0, the deformation remains almost elastic in the first loading-unloading stage and the loading path is almost on top of the unloading path. However, during the second loading-unloading cycle, the inclusion starts to detach from the matrix which leads to softening of the material and a sudden drop in the effective response. At this point, the damage parameter \mathcal{D} approaches quickly to 1. By the end of the second loading stage, the inclusion and the interface do not contribute anymore to the overall response. Therefore, during the third loading-unloading phase, only the matrix is deformed resulting in a pure elastic deformation. Next, $\bar{\mu}$ is set to 25 and as we expect, larger effective responses are obtained for all the deformation stages while the behavior of the material remains qualitatively identical to previous case. However, we note that increasing $\bar{\mu}$ postpones the failure of the material to a larger deformation. Finally, $\bar{\mu}$ is set to 1000 making it considerably stiffer against the deformations along the interface. Obviously, greater resistance against the deformation along the interface makes the interface capable of keeping the inclusion and the matrix next to each other and eventually avoiding the material from failure.

4.3 Three-dimensional example

In order to investigate the interface effects in a three-dimensional example and demonstrate the generality of the presented framework, a similar study is conducted, as shown in Fig. 12. For this set of study, we prescribe 150% of volumetric expansion on the boundary of the spherical unit-cell and investigate the change in the effective response as well as the damage parameter for various values of $\bar{\mu}$ while cohesive interface parameters are kept constant. It is observed that,

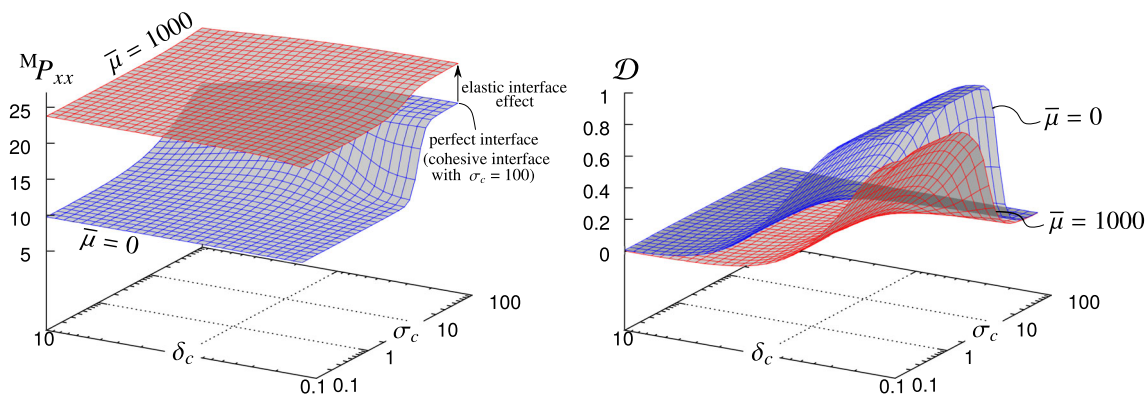


Fig. 10 xx -component of the macroscopic Piola stress (left) and damage parameter (right) with varying δ_c and σ_c when the inclusion and the matrix are of the same type. Different surfaces represent the results for different values of elastic interface material parameter $\bar{\mu}$. When

$\sigma_c = 100$, the cohesive interface behaves like a perfect interface. However, increasing the elastic interface parameter introduces additional stresses and yields stiffer overall response which can not be recovered by the cohesive interface model

similar to the results from the two-dimensional microstructure, increasing $\bar{\mu}$ from 0 to 10 leads to postponing the failure point to larger deformations. Moreover, larger $\bar{\mu}$ yields a smaller damage parameter for all the deformation stages. It is also confirmed that setting the elastic interface material parameter to a large value, here $\bar{\mu} = 100$, avoids accumulation of damage on the interface by firmly keeping the inclusion and the matrix next to each other. Overall, the trend of the results is qualitatively quite close to what is observed for two-dimensional microstructure and the conclusions made based on the results from the two-dimensional microstructure also hold for three-dimensional simulations.

4.4 Size-effect

Endowing the unit-cell with an interface introduces a length scale into the problem and leads to a size-dependent response, often referred to as the size-effect. This section aims to study the size-effects due to various interface models. Here, the inclusion and the matrix are assumed to be identical. We prescribe 100% volumetric expansion on the boundary of the spherical unit-cell and examine the change in the size-dependent response as $\bar{\mu}$ increases. The cohesive interface material parameters are set to $\sigma_c = 12$ and $\delta_c = 0.2$. For comparison, we additionally present the results when interface damage is excluded. For this case, it is assumed that the orthogonal response of the interface is governed by the linear traction-separation law $\{\{t\}\} = \sigma_c / \delta_c \llbracket \varphi \rrbracket$. As depicted in Fig. 13, when $\bar{\mu} = 0$, an elastic interface does not result in any size-effect and resembles a perfect interface model. Additionally, whether or not interface damage is considered, the general interface reduces to the cohesive interface and the results overlap. When damage is considered, both general and cohesive interfaces exhibit a larger-stiffer response only up to a certain point (size = 0.2) which is followed

by an abrupt drop and full damage of the interface. This is due to the fact that, when the size of the unit-cell increases, the critical opening displacement on the cohesive interface ($\delta_c = 0.2$) may be reached for smaller deformations leading to the full interface damage for larger sizes. Increasing the elastic interface material parameter $\bar{\mu}$, on the one hand, leads to capturing the smaller-stronger size-effect from the elastic interface, and on the other hand leads to postponing the full interface damage on the general interface to larger sizes. Clearly, changing the elastic interface parameter does not influence the results obtained from the cohesive interface model. Note that if the interface damage is excluded and for very large unit-cells, all the interface models capture the same overall response as the interface effects become negligible. Such behavior may not be observed if the interface damage is considered though.

4.5 Influence of boundary conditions

This section aims to provide a comprehensive comparison on the results obtained from different boundary conditions when a general interface is taken into account. First, in order to set up the stage, we conduct the analysis on a rectangular unit-cell. Next, we add to the morphological complexity of the sample and investigate more realistic microstructures. In addition to the boundary condition effect, the effects of size and distribution pattern of the inclusions on the overall response are studied.

Figure 14 depicts the change in overall response of the rectangular unit-cell calculated based on DBC, PBC and TBC as the sample undergoes 200% of volumetric expansion deformation. This study is carried out for fixed cohesive interface material parameters and for three elastic interface material parameters, namely $\bar{\mu} = 0, 10, 15$. In this section, it is assumed that the inclusion and the matrix are of the

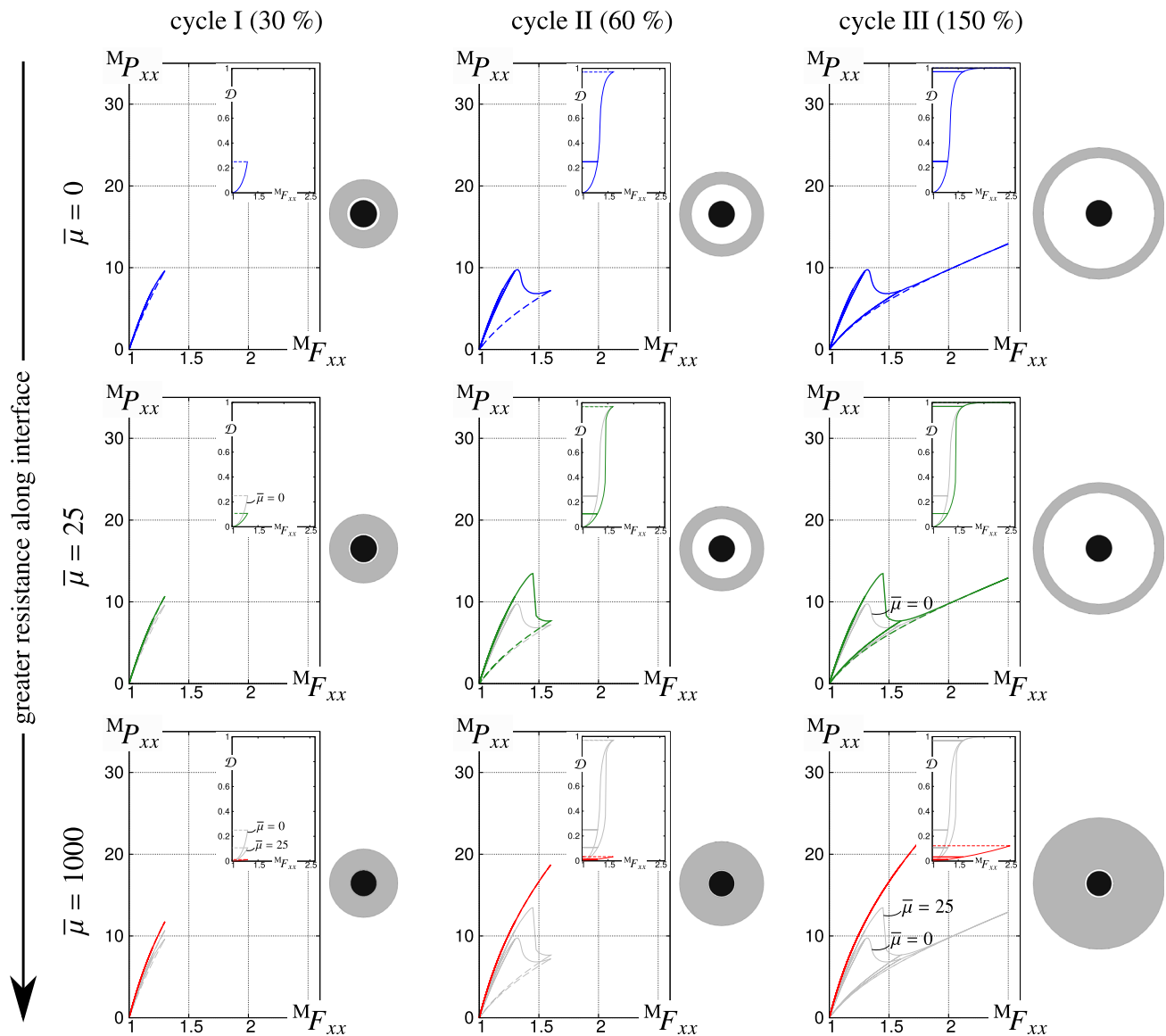


Fig. 11 xx -component of macroscopic Piola stress with respect to increasing and decreasing the prescribed deformation. The solid lines and the dashed lines in the figures represent the loading phase and the unloading phase, respectively. In addition, change in the damage param-

eter evaluated at a point on the interface is depicted as inserts confirming irreversibility of damage ($D \geq 0$). The deformation of the unit-cell at the last point of each plot is also shown next to the plots

same type. Numerical results confirm that, in accordance to what is observed in purely elastic problems, the results from PBC lie between the results of the two other boundary conditions with DBC and TBC providing overestimated and underestimated response, respectively. Moreover, it is observed that all the boundary conditions estimate almost the same deformation value for the failure point with DBC and TBC estimating slightly smaller and larger deformations as the starting point for the failure. It is worth noting that, while the results from different boundary conditions remain quite close to each other before the failure point, they provide significantly different responses afterwards. Clearly, after the

full decohesion of the inclusion from the matrix, interface effects are eliminated as well. This case is equivalent to a rectangular RVE with a circular void at its center. Therefore, effective responses obtained from different boundary conditions would be independent of $\bar{\mu}$ and coincide with the ones obtained for a unit-cell with a void at its center. In view of the deformations illustrated in Fig. 14, although the unit-cells corresponding to DBC and PBC look nearly identical, their associated effective responses differ as can be seen on the plot next to the depicted unit-cells. This is due to the fact that the geometrical differences between DBC and PBC are subtle but yet they influence the resulting stress distributions somewhat

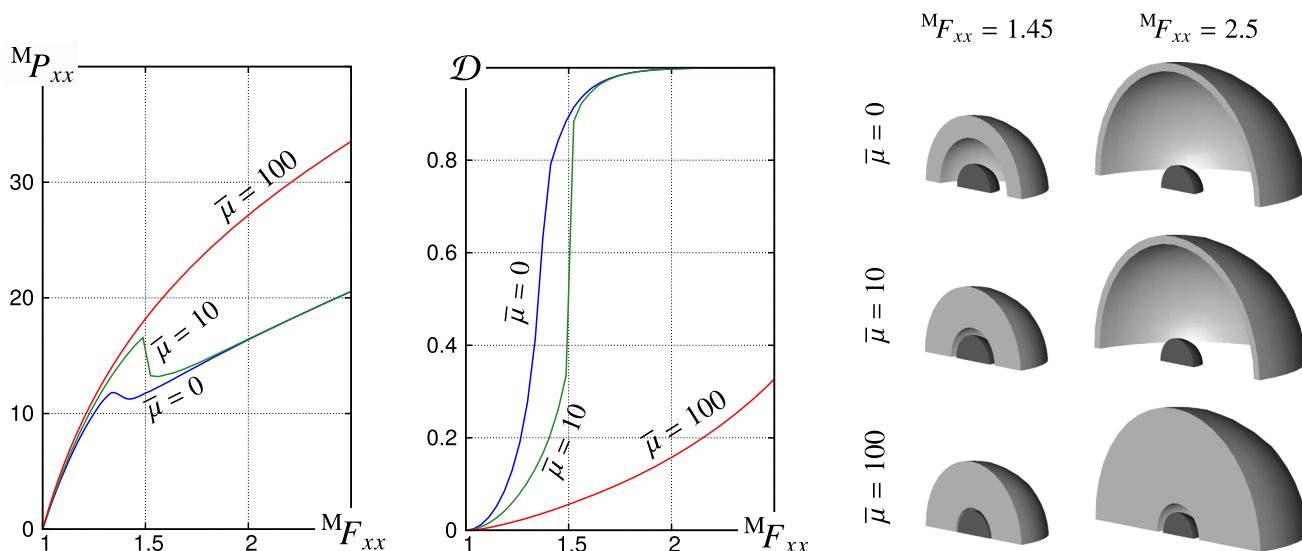


Fig. 12 xx -component of macroscopic Piola stress and damage parameter with respect to increasing the prescribed deformation for spherical unit-cell. The figures next to the plot depict the deformation of the unit-cell at 45 and 150% of deformation for different values of $\bar{\mu}$. For clarity purposes, one fourth on the spherical unit-cell is shown

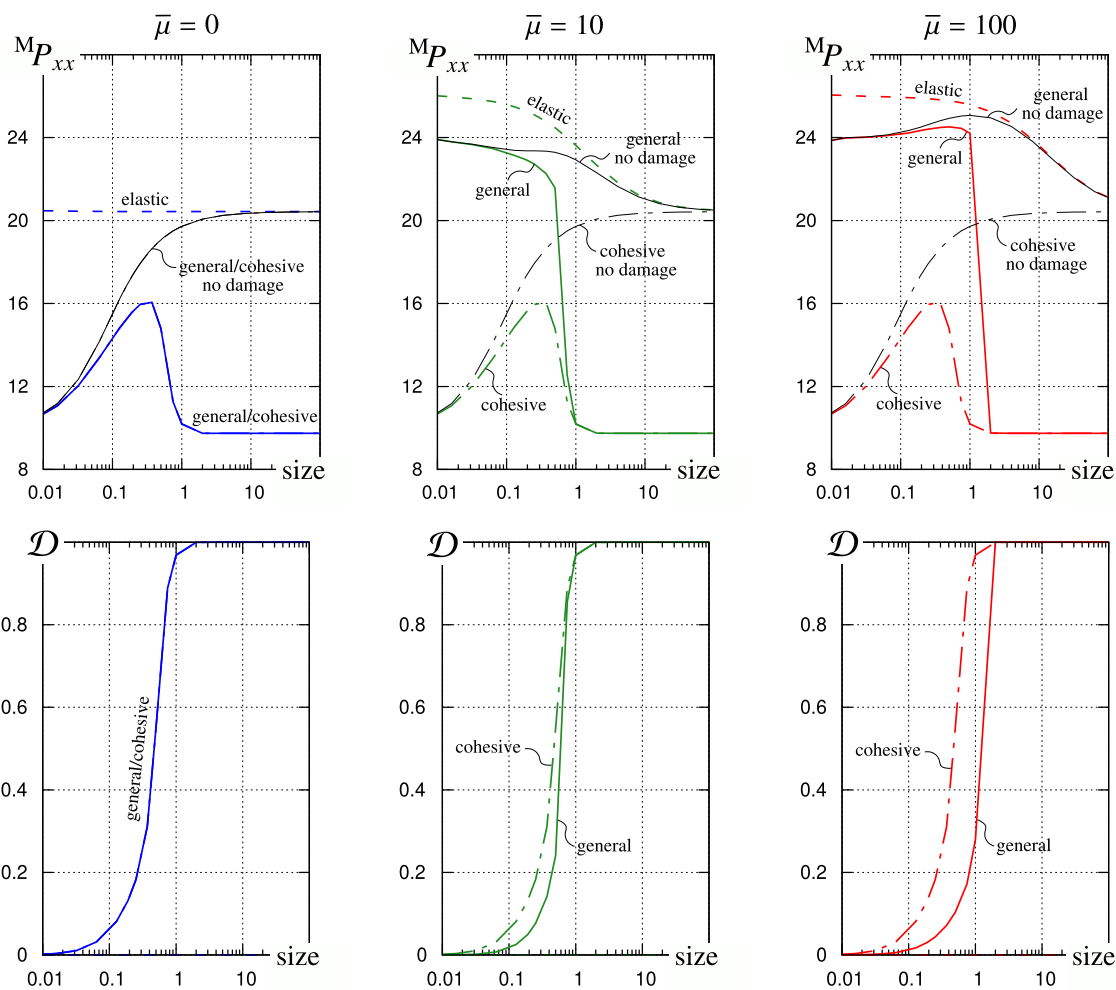


Fig. 13 Size-effects captured by different interface models for different elastic interface material parameters

significantly. The deformed configurations depicted on the right side of the plot correspond to 75% volumetric expansion and no substantial damage is accumulated on the interface. Having a closer look to the deformations, we see that for non-zero values of $\bar{\mu}$, the inclusion experiences a compression and shrinks. The shrinkage of the inclusion is a consequence of the elastic interface and the assumption that the interface lies on the mid-surface, i.e. $\bar{\mathbf{x}} = \{\{\mathbf{x}\}\}$. See [42] for detailed discussions on rationale behind this choice. Obviously, after the full decohesion, the interface effects are eliminated and the inclusion regains its initial shape. We additionally point out that the results presented in this manuscript shall be considered as only numerical studies covering a broad range of parameters which may or may not represent the real world materials discovered and designed thus far. From a mathematical perspective though, the chosen material parameters for elastic interface are admissible and satisfy point-wise stability and ellipticity, see [97]. Moreover, material modeling of bulk materials is a mature field with many standard references. This is not the case for the general interface though. There have been a number of theoretical studies on general interfaces, but there are very few experiments for measuring the materials constants. Nevertheless, in the opinion of the authors without a clear theoretical understanding of suitable models no experimental evidence may be obtained. We recall that the controversy about the true number of coefficients in isotropic elasticity (Navier believed that only one was sufficient) was first clarified theoretically by Lamé and only then it was possible to measure the material constants. We believe that sooner or later general interface material parameters introduced by well-posed theories will be measured.

Next, we perform a similar study on more complicated microstructures depicted in Fig. 15. All the microstructures contain 16 inclusions in 4 different sizes adding up to 20% volume fraction. In the microstructure (A), the largest inclusions are located close to the four corners whereas smaller inclusions are distributed randomly within the matrix. In the microstructure (B), the largest inclusions are packed at the center with smaller inclusions being distributed randomly elsewhere. In the microstructure (C), all the inclusions are distributed randomly without following any specific order. Similar to the unit-cell analysis, we investigate the change in overall response of different microstructures DBC, PBC and TBC under 200% volumetric expansion. This study is carried out for cohesive interface material parameters $\sigma_c = 3$ and $\delta_c = 0.05$ and for three elastic interface material parameters $\bar{\mu} = 0, 8, 10$. The inclusion-to-matrix stiffness ratio is 10 for all the examples.

The rows in Fig. 16 correspond to the results associated with DBC, PBC and TBC for the above-mentioned microstructures. We observe that for all the boundary conditions and all the microstructures when $\bar{\mu} = 0$ the overall response remains smooth although several inclu-

sions undergo debonding. Setting non-zero values for $\bar{\mu}$ brings several abrupt changes in the overall response of the microstructures though. The numerical results show that regardless of the boundary condition employed and the inclusion distribution pattern, increasing $\bar{\mu}$ stiffens the overall response and more importantly, delays the failure points. This is in accordance with the observations we made earlier for the unit-cell. In addition, it is observed that, in all the cases, decohesion takes place first on the interfaces of the larger inclusions. This is in agreement with the results reported in the literature based on experimental studies [98,99] and numerical analysis [89,100] although for a cohesive interface model. The plots on the first row indicates that when DBC is employed and for $\bar{\mu} = 8$, after the initial failure on interfaces of the 4 largest inclusions, further increase of the deformation triggers a secondary failure on the interfaces of smaller inclusions leading to softening of the overall response. The secondary failure deformation strongly depends on the inclusion distribution pattern and differs from one microstructure to another. More specifically, it starts at $^M F_{xx} = 2.75$ for the center-biased, at $^M F_{xx} = 2.55$ for the corner-biased and at $^M F_{xx} = 2.65$ for the random microstructure. For $\bar{\mu} = 10$, the smaller inclusions in the center-biased microstructure remain bonded even for larger deformations while the smaller inclusions in other microstructures experience debonding from the matrix. The second row exhibits the results for PBC. For $\bar{\mu} = 8$ a secondary failure stage begins within all three microstructures as the deformation increases. However, the deformation for the secondary failure point is larger than the ones associated with DBC. That is, after the decohesion on interfaces of the 4 largest inclusions, the smaller inclusions remain bonded for larger deformations under PBC than under DBC. Moreover, it is shown that for $\bar{\mu} = 10$, the smaller inclusions remain bonded even for larger deformations which is in contrast to the results obtained from DBC. The last row represents the results corresponding to TBC for which the deformations are somewhat unfamiliar and sensitive to the positions of the large inclusions. Nevertheless, as it will be discussed later, the overall response remains similar to those from DBC and PBC. The numerical results show that for the center-biased microstructure and $\bar{\mu} = 8$, a secondary failure stage begins as a result of debonding of the small inclusions close to the boundary. However, regardless of the value of $\bar{\mu}$, we observe no debonding of the smaller inclusions in the corner-biased and random microstructures. This is mainly due to the fact that, after the initial decohesion of the large inclusions close to the boundary, the compliant matrix around the large inclusions can significantly deform. Clearly, this cannot be the case for DBC and PBC which requires prescribing the deformation on the boundary. As a result, TBC, in general, leads to debonding on fewer smaller inclusions as compared to DBC and PBC. Similarly, PBC, in general, leads to debonding on fewer smaller inclusions than

Fig. 14 Comparison of the effective responses obtained from different boundary conditions. While the results remain close to each other before the failure point, they provide considerably different responses afterwards with DBC and TBC providing overestimated and underestimated responses compared to PBC. The figures on the right depict the deformation obtained for different boundary conditions when 75% of volumetric expansion is prescribed

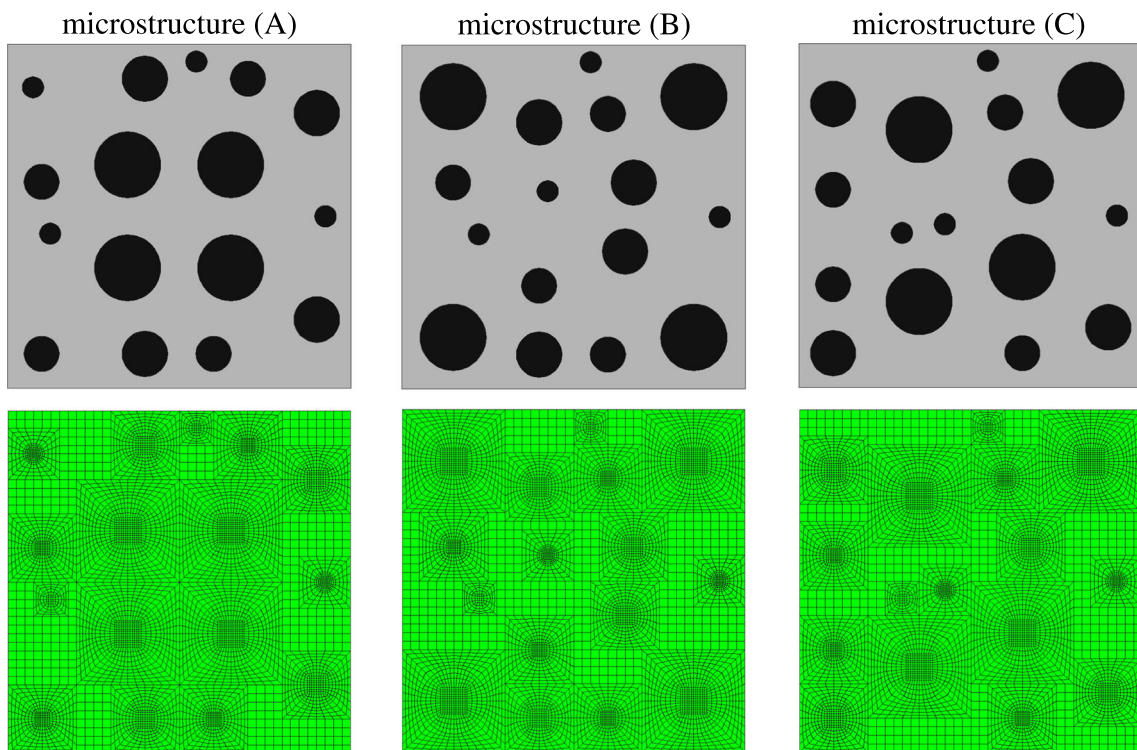
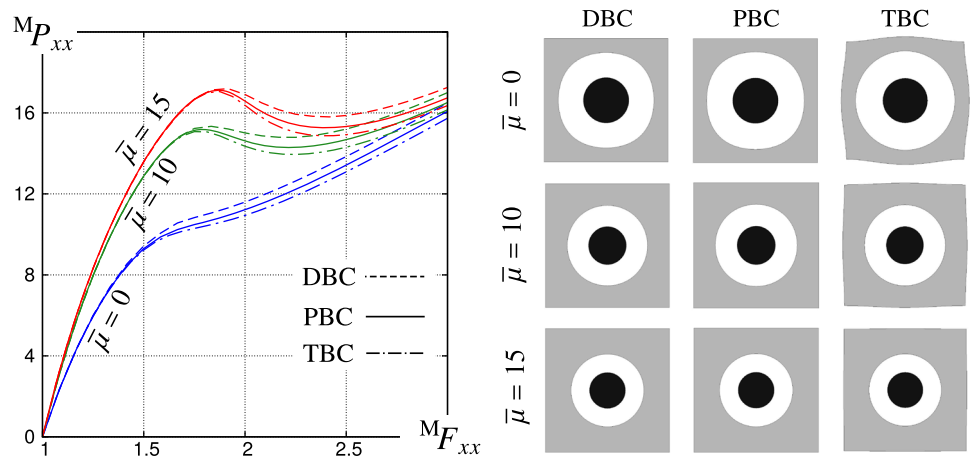


Fig. 15 Three microstructures with different inclusion distribution patterns are employed to conduct the numerical analysis. The microstructures are different particularly in the positions of the 4 largest inclusions.

Due to this reason, we commonly refer to them as center-biased, corner-biased and random microstructures

DBC. Such behavior in turn leads to an interesting observation depicted in Fig. 17 which compares the overall responses obtained from different boundary conditions for microstructures (A), (B) and (C) when $\bar{\mu} = 8$. It is shown that up to the initial failure stage, the results are independent of the choice of the boundary condition. All the three boundary conditions estimate almost the same deformation as the initial failure point for the center-biased microstructure. This is in accordance with our expectation as the large inclusions (i.e. the first ones to debond), are far from the boundary leading to insignificant boundary effects. For the other two

microstructures though, DBC and PBC provide exactly the same failure deformation whereas TBC estimates a smaller value. Subsequently, each boundary condition provides a different sequence for debonding on the interfaces of the large inclusions. By further increasing the deformation, the results from PBC remain mostly between the results from the other two boundary conditions with DBC and TBC providing overestimated and underestimated response, respectively. An exception can be found in the results of the center-biased microstructure though. By increasing of the deformation and approaching the secondary failure points, it becomes clear

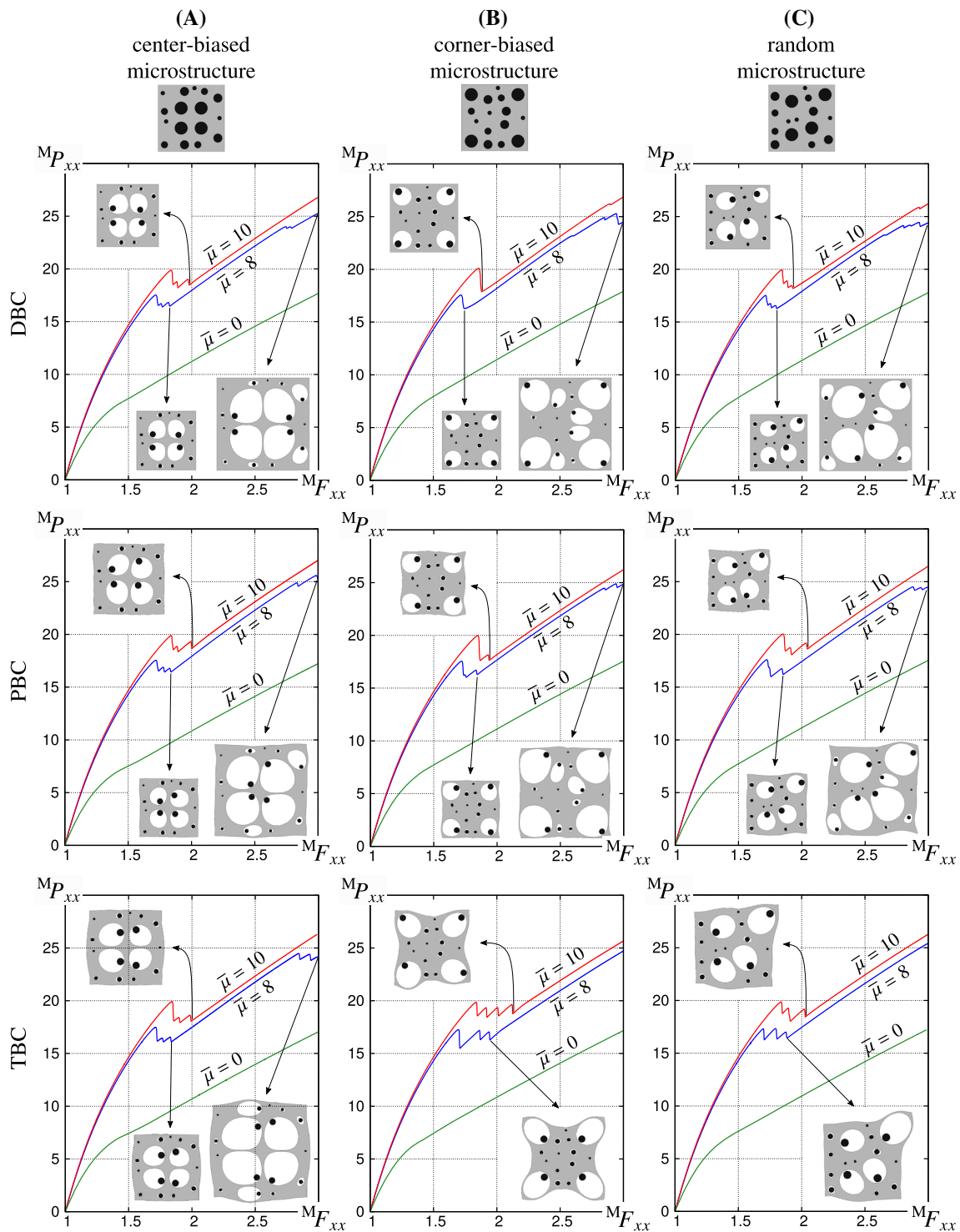


Fig. 16 Comparison of the effective response obtained from different boundary conditions for the microstructures depicted in Fig. 15

that earlier occurrence of secondary failure under DBC leads to a softer overall response as compared to TBC and in some cases PBC. This is in contrast to what is commonly observed in purely elastic problems. Clearly, such a drastic influence of the boundary conditions on the overall response stems

from the fact that none of the microstructures studied in this section is representative.

Computational simulations for such complicated geometries and broad set of parameters in the presence of abrupt softening within the microstructure along with the highly

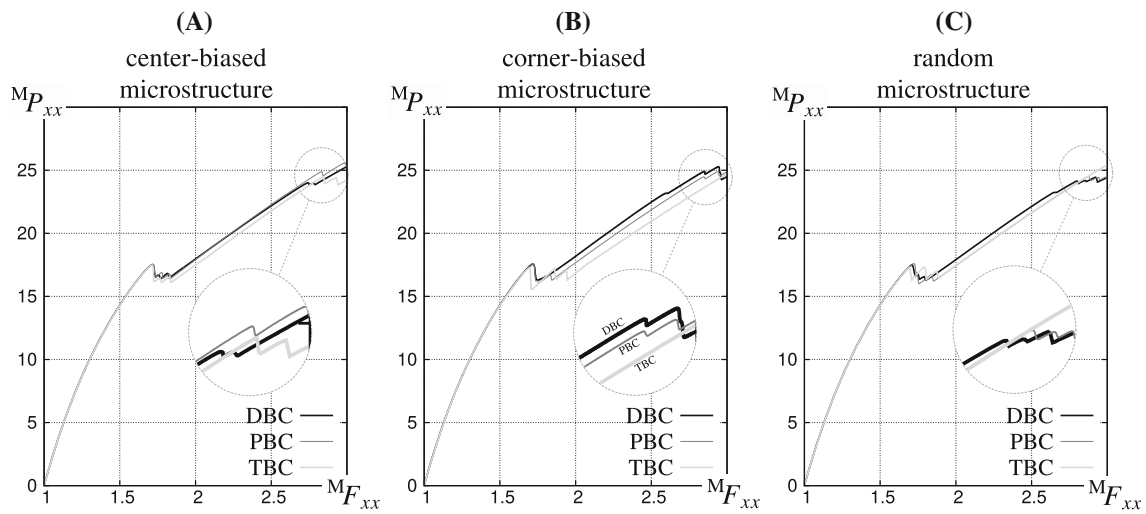


Fig. 17 Comparison of the results obtained from different boundary conditions. It is demonstrated that the results from DBC underestimates the results from TBC for sufficiently deformation due to earlier occurrence of debonding on smaller inclusions

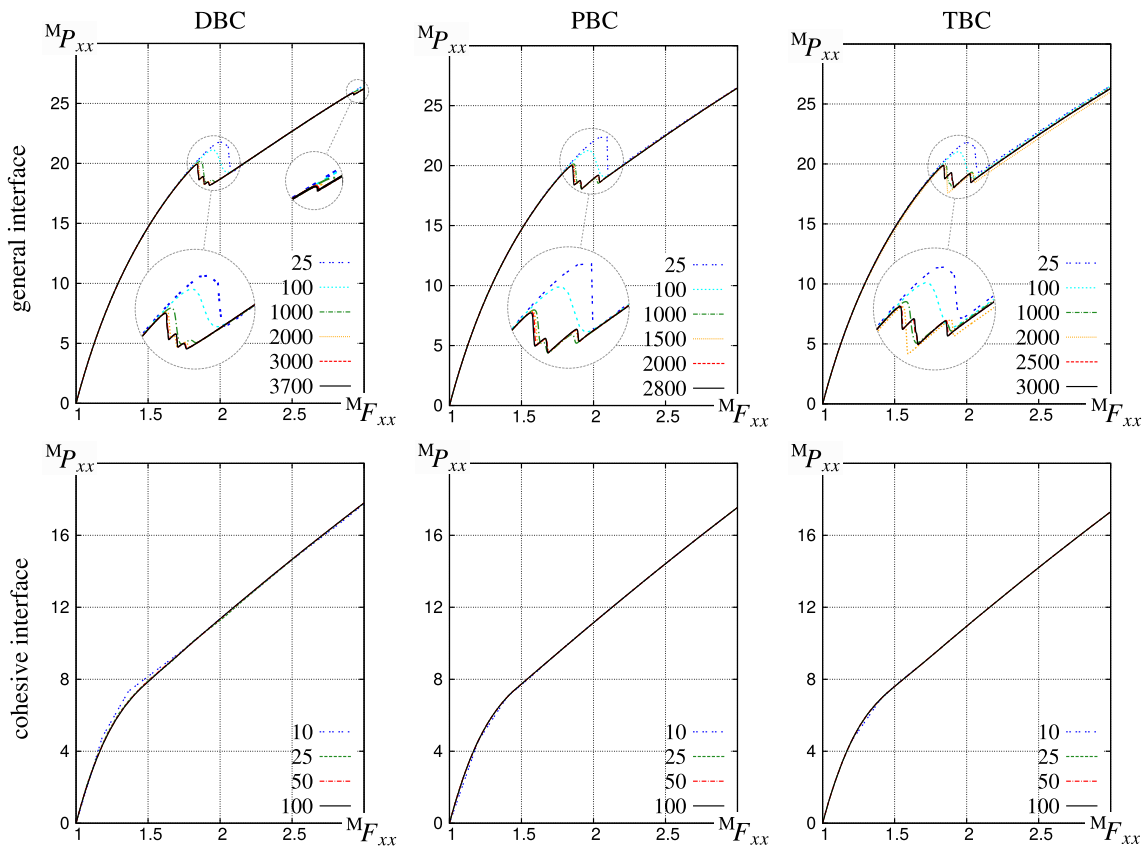


Fig. 18 Illustration of the convergence of the results to a unique solution by increasing of the number of increments. The results depicted at the top correspond to the random microstructure with $\bar{\mu} = 10$ and the ones depicted at the bottom correspond to the random microstructure with $\bar{\mu} = 0$

complex interaction of the inclusions demonstrates the robustness of the presented framework. In order to investigate the validity of the results and to ensure the consistency of the framework, we have additionally examined the convergence of the results under different boundary conditions

with respect to the number of increments, as given in Fig. 18. For the cohesive interface model, even very small number of increments leads to convergence of the results to a unique solution. This is clearly due to the fact that no abrupt softening takes place and the overall response remains sufficiently

smooth. For non-zero values of $\bar{\mu}$, utilizing a small number of increments may lead to overlooking all or some of the critical points along the equilibrium path resulting in an inaccurate response. Increasing the number of increments leads to convergence of the results to a unique solution proving the reliability of the developed scheme. For each set of the simulations presented throughout the paper, we have performed a similar study and have chosen the converged result. Note that the smooth behavior observed for $\bar{\mu} = 0$ is mainly associated with the chosen cohesive interface parameters. A different set of parameters could have led to severe changes in the local and overall response that would demand larger number of increments in the solution procedure.

5 Conclusion

A computational framework to study the effective response of microstructures in the presence of general interfaces equipped with damage is presented. Pertinent computational aspects have been reviewed. A systematic study on the influence of different interface material parameters associated with elastic and cohesive interface models on the effective response of several unit-cells subject to volumetric expansion is presented. Both two- and three-dimensional examples have been considered. The numerical results reveal that increasing the elasticity along the interface leads to stiffening across the interface. In particular, it is observed that larger elastic interface material parameter leads to postponing the failure point and ultimately, prevents the accumulation of damage regardless of the cohesive interface material parameters. Moreover, a thorough comparison on the influence of different boundary conditions on the overall response is given. The unit-cell analysis demonstrates that in accordance to what is observed in the classical computational homogenization, the results from PBC lie between the results associated with DBC and TBC. However, the results of the random microstructures do not completely follow this pattern. More precisely, in the presence of general interfaces with damage, DBC and TBC do not provide the bounds for random microstructures as they do in purely elastic problems.

Acknowledgements The support of this work by the Cluster of Excellence “Engineering of Advanced Materials” at the University of Erlangen–Nuremberg, funded by the DFG within the framework of its “Excellence Initiative”, is greatly appreciated.

References

- Sharma P, Ganti S (2004) Size-dependent Eshelby’s tensor for embedded nano-inclusions incorporating surface/interface energies. *J Appl Mech* 71(5):663–671
- Dingreville R, Qu J, Cherkaoui M (2005) Surface free energy and its effect on the elastic behavior of nano-sized particles, wires and films. *J Mech Phys Solids* 53(8):1827–1854
- He J, Lilley CM (2008) Surface effect on the elastic behavior of static bending nanowires. *Nano Lett* 8:1798–1802
- Mogilevskaya SG, Crouch SL, Stolarski HK (2008) Multiple interacting circular nano-inhomogeneities with surface/interface effects. *J Mech Phys Solids* 56(6):2298–2327
- Cheng YT, Verbrugge MW (2008) The influence of surface mechanics on diffusion induced stresses within spherical nanoparticles. *J Appl Phys* 104(8):083521
- Wang ZQ, Zhao YP, Huang ZP (2010) The effects of surface tension on the elastic properties of nano structures. *Int J Eng Sci* 48(2):140–150
- Ansari R, Sahmani S (2011) Bending behavior and buckling of nanobeams including surface stress effects corresponding to different beam theories. *Int J Eng Sci* 49(11):1244–1255
- Altenbach H, Eremeyev VA (2011) On the shell theory on the nanoscale with surface stresses. *Int J Eng Sci* 49(12):1294–1301
- Park H (2012) Surface stress effects on the critical buckling strains of silicon nanowires. *Comput Mater Sci* 51:396–401
- Nanthakumar SS, Valizadeh N, Park HS, Rabczuk T (2015) Surface effects on shape and topology optimization of nanostructures. *Comput Mech* 56:97–112
- Cordero NM, Forest S, Busso EP (2016) Second strain gradient elasticity of nano-objects. *J Mech Phys Solids* 97:92–124
- Chatzigeorgiou G, Meraghni F, Javili A (2017) Generalized interfacial energy and size effects in composites. *J Mech Phys Solids* 106:257–282
- Barenblattm GI (1962) The mathematical theory of equilibrium cracks in brittle fracture. *Adv Appl Mech* 7:55–129
- Hillerborg A, Mod er M, Petersson P-E (1976) Analysis of crack formation and crack growth in concrete by means of fracture mechanics and finite elements. *Cem Concrete Res* 6:773–781
- Xu X-P, Needleman A (1994) Numerical simulations of fast crack growth in brittle. *J Mech Phys Solids* 42:1397–1434
- Ortiz M, Pandolfi A (1999) Finite-deformation irreversible cohesive elements for three-dimensional crack-propagation analysis. *Int J Numer Methods Eng* 44:1267–1282
- Javili A (2018) A note on traction continuity across an interface in a geometrically non-linear framework. *Math Mech Solids*. <https://doi.org/10.1177/1081286518766980>
- Wells GN, Sluys LJ (2001) A new method for modelling cohesive cracks using finite elements. *Int J Numer Methods Eng* 50:2667–2682
- Rommers JJC, de Borst R, Needleman A (2003) A cohesive segments method for the simulation of crack growth. *Comput Mech* 31:69–77
- Zhou F, Molinari JF (2003) Dynamic crack propagation with cohesive elements: a methodology to address mesh dependency. *Int J Numer Methods Eng* 59:1–24
- Mergheim J, Kuhl E, Steinmann P (2005) A finite element method for the computational modelling of cohesive cracks. *Int J Numer Methods Eng* 63:276–289
- van den Bosch MJ, Schreurs PJG, Geers MGD (2006) An improved description of the exponential Xu and Needleman cohesive zone law for mixed-mode decohesion. *Eng Fract Mech* 73:1220–1234
- van den Bosch MJ, Schreurs PJG, Geers MGD (2007) On the development of a 3d cohesive zone element in the presence of large deformations. *Comput Mech* 42:171–180
- Terada K, Ishii T, Kyoya T, Kishino Y (2007) Finite cover method for progressive failure with cohesive zone fracture in heterogeneous solids and structures. *Comput Mech* 191–210:2007

25. Ural A, Krishnan VR, Papoulia KD (2009) A cohesive zone model for fatigue crack growth allowing for crack retardation. *Int J Solids Struct* 46:2453–2462
26. Park K, Paulino GH, Roesler JR (2009) A unified potential-based cohesive model of mixed-mode fracture. *J Mech Phys Solids* 57:891–908
27. Yang QD, Fang XJ, Shi JX, Lua J (2010) An improved cohesive element for shell delamination analyses. *Int J Numer Methods Eng* 83:611–641
28. Needleman A (2014) Some issues in cohesive surface modeling. *Proc IUTAM* 10:221–246
29. Dimitri R, De Lorenzis L, Wriggers P, Zavarise G (2014) NURBS- and T-spline-based isogeometric cohesive zone modeling of interface debonding. *Comput Mech* 54:369–388
30. Moeckel GP (1975) Thermodynamics of an interface. *Arch Ration Mech Anal* 57:255–280
31. Murdoch AI (1976) A thermodynamical theory of elastic material interfaces. *Q J Mech Appl Math* 29(3):245–275
32. dell’Isola F, Romano A (1987) On the derivation of thermo-mechanical balance equations for continuous systems with a nonmaterial interface. *Int J Eng Sci* 25:1459–1468
33. Fried E, Gurtin ME (2007) Thermomechanics of the interface between a body and its environment. *Contin Mech Thermodyn* 19:253–271
34. Javili A, Ottosen NS, Ristinmaa M, Mosler J (2017a) Aspects of interface elasticity theory. *Math Mech Solids* 23:1004–1024
35. Gurtin ME, Murdoch AI (1975) A continuum theory of elastic material surfaces. *Arch Ration Mech Anal* 57(4):291–323
36. Duan HL, Wang J, Karihaloo BL (2009) Theory of elasticity at the nanoscale. *Adv Appl Mech* 42:1–68
37. Javili A, McBride A, Steinmann P (2013a) Thermomechanics of solids with lower-dimensional energetics: on the importance of surface, interface, and curve structures at the nanoscale. A unifying review. *Appl Mech Rev* 65:010802
38. Hashin Z (2002) Thin interphase/imperfect interface in elasticity with application to coated fiber composites. *J Mech Phys Solids* 50:2509–2537
39. Benveniste Y, Miloh T (2003) Imperfect soft and stiff interfaces in two-dimensional elasticity. *Mech Mater* 33:309–323
40. Steinmann P, Häsner O (2005) On material interfaces in thermo-mechanical solids. *Arch Appl Mech* 75:31–41
41. Monchiet V, Bonnet G (2010) Interfacial models in viscoplastic composites materials. *Int J Eng Sci* 48:1762–1768
42. Javili A, Steinmann P, Mosler J (2017b) Micro-to-macro transition accounting for general imperfect interfaces. *Comput Methods Appl Mech Eng* 317:274–317
43. Javili A (2017) Variational formulation of generalized interfaces for finite deformation elasticity. *Math Mech Solids* 23:1303–1322
44. Heitbreder T, Ottosen NS, Ristinmaa M, Mosler J (2018) On damage modeling of material interfaces: Numerical implementation and computational homogenization. *Comput Methods Appl Mech Eng* 337:1–27
45. Javili A, Käsmair S, Steinmann P (2014a) General imperfect interfaces. *Comput Methods Appl Mech Eng* 275:76–97
46. Esmaeili A, Javili A, Steinmann P (2017) Coupled thermally general imperfect and mechanically coherent energetic interfaces subject to in-plane degradation. *J Mech Mater Struct* 12:289–312
47. Pavanello F, Manca F, Luca Palla P, Giordano S (2012) Generalized interface models for transport phenomena: unusual scale effects in composite nanomaterials. *J Appl Phys* 112:084306
48. Miehe C, Koch A (2002) Computational micro-to-macro transitions of discretized microstructures undergoing small strains. *Arch Appl Mech* 72:300–317
49. Guidault PA, Allix O, Champaney L, Navarro JP (2007) A two-scale approach with homogenization for the computation of cracked structures. *Comput Struct* 85:1360–1371
50. Danas K, Idiart MI, Ponte Castañeda P (2008) A homogenization-based constitutive model for isotropic viscoplastic porous media. *Int J Solids Struct* 45:3392–3409
51. Hain M, Wriggers P (2008) Computational homogenization of micro-structural damage due to frost in hardened cement paste. *Finite Elem Anal Des* 44:233–244
52. Inglis HM, Geubelle PH, Matouš K (2008) Boundary condition effects on multiscale analysis of damage localization. *Philos Mag* 88:2373–2397
53. Temizer İ, Wriggers P (2008) On the computation of the macroscopic tangent for multiscale volumetric homogenization problems. *Comput Methods Appl Mech Eng* 198:495–510
54. Özdemir I, Brekelmans WAM, Geers MGD (2008) FE² computational homogenization for the thermo-mechanical analysis of heterogeneous solids. *Comput Methods Appl Mech Eng* 198:602–613
55. Geers MGD, Kouznetsova VG, Brekelmans WAM (2010) Multi-scale computational homogenization: trends and challenges. *J Comput Appl Math* 234:2175–2182
56. Terada K, Kurumatani M, Ushida T, Kikuchi N (2010) A method of two-scale thermo-mechanical analysis for porous solids with micro-scale heat transfer. *Comput Mech* 46:269–285
57. Larsson F, Runesson K, Saroukhani S, Vafadari R (2011) Computational homogenization based on a weak format of micro-periodicity for RVE-problems. *Comput Methods Appl Mech Eng* 200:11–26
58. Coenen EWC, Kouznetsova VG, Bosco E, Geers MGD (2012) A multi-scale approach to bridge microscale damage and macroscale failure: a nested computational homogenization-localization framework. *Int J Fract* 178:157–178
59. Kochmann DM, Venturini GN (2013) Homogenized mechanical properties of auxetic composite materials in finite-strain elasticity. *Smart Mater Struct* 22:084004
60. Javili A, Chatzigeorgiou G, Steinmann P (2013b) Computational homogenization in magneto-mechanics. *Int J Solids Struct* 50:4197–4216
61. Bosco E, Kouznetsova VG, Geers MGD (2015) Multi-scale computational homogenization-localization for propagating discontinuities using X-FEM. *Int J Numer Methods Eng* 102:496–527
62. Cong Y, Nezamabadi S, Zahrouni H, Yvonnet J (2015) Multiscale computational homogenization of heterogeneous shells at small strains with extensions to finite displacements and buckling. *Int J Numer Methods Eng* 104:235–259
63. Alberdi R, Zhang G, Khandelwal K (2018) A framework for implementation of RVE based multiscale models in computational homogenization using isogeometric analysis. *Int J Numer Methods Eng* 114:1018–1051
64. Eidel B, Fischer A (2018) The heterogeneous multiscale finite element method for the homogenization of linear elastic solids and a comparison with the FE² method. *Comput Methods Appl Mech Eng* 329:332–368
65. Kanouté P, Boso DP, Chaboche JL, Schrefler BA (2009) Multi-scale methods for composites: a review. *Arch Comput Methods Eng* 16:31–75
66. Charalambakis N (2010) Homogenization techniques and micromechanics. A survey and perspectives. *Appl Mech Rev* 63:030803
67. Saeb S, Steinmann P, Javili A (2016) Aspects of computational homogenization at finite deformations: a unifying review from reuss’ to voigt’s bound. *Appl Mech Rev* 68(5):050801
68. Matouš K, Geers MGD, Kouznetsova VG, Gillman A (2017) A review of predictive nonlinear theories for multiscale modeling of heterogeneous materials. *J Comput Phys* 330:192–220
69. Greer JR, Oliver WC, Nix WD (2005) Size dependence of mechanical properties of gold at the micron scale in the absence of strain gradients. *Acta Mater* 53:1821–1830

70. Taloni A, Vodret M, Costantini G, Zapperi S (2018) Size effects on the fracture of microscale and nanoscale materials. *Nat Rev Mater* 3:211–224
71. Kouznetsova VG, Geers MGD, Brekelmans WAM (2004) Multiscale second-order computational homogenization of multi-phase materials: a nested finite element solution strategy. *Comput Methods Appl Mech Eng* 193:5525–5550
72. Kaczmarczyk L, Pearce CJ, Bićanić N (2008) Scale transition and enforcement of RVE boundary conditions in second-order computational homogenization. *Int J Numer Methods Eng* 74:506–522
73. Matouš K, Geubelle PH (2005) Multiscale modelling of particle debonding in reinforced elastomers subjected to finite deformations. *Int J Numer Methods Eng* 65:190–223
74. Fritzen F, Leuschner M (2015) Nonlinear reduced order homogenization of materials including cohesive interfaces. *Comput Mech* 56:131–151
75. Spring DW, Paulino GH (2015) Computational homogenization of the debonding of particle reinforced composites: the role of interphases in interfaces. *Comput Mater Sci* 109:209–224
76. Toro S, Sánchez PJ, Blanco PJ, de Souza Neto EA, Huespe AE, Feijóo RA (2016) Multiscale formulation for material failure accounting for cohesive cracks at the macro and micro scales. *Int J Plast* 76:75–110
77. Yvonnet J, Quang H Le, He Q-C (2008) An XFEM/level set approach to modelling surface/interface effects and to computing the size-dependent effective properties of nanocomposites. *Comput Mech* 42(1):119–131
78. Javili A, Chatzigeorgiou G, McBride A, Steinmann P, Linder C (2015) Computational homogenization of nano-materials accounting for size effects via surface elasticity. *GAMM Mitteilungen* 38:285–312
79. Wilmers J, McBride A, Bargmann S (2017) Interface elasticity effects in polymer-filled nanoporous metals. *J Mech Phys Solids* 99:163–177
80. McBride A, Mergheim J, Javili A, Steinmann P, Bargmann S (2012) Micro-to-macro transitions for heterogeneous material layers accounting for in-plane stretch. *J Mech Phys Solids* 60:1221–1239
81. Dargazany R, Itskov M (2013) Constitutive modeling of the mullins effect and cyclic stress softening in filled elastomers. *Phys Rev E* 88:012602
82. Bueche F (1961) Mullins effect and rubber–filler interaction. *Appl Polym* 5:271–281
83. Kilian HG, Strauss M, Hamm W (1994) Universal properties in filler-loaded rubbers. *Rubber Chem Technol* 67:1–16
84. Govindjee S, Simo J (1992) Transition from micro-mechanics to computationally efficient phenomenology: Carbon black filled rubbers incorporating Mullins' effect. *Journal of the Mechanics and Physics of Solids* 40:213–233
85. Ogden RW, Roxburgh DG (1999) A pseudo-elastic model for the Mullins effect in filled rubber. *Proc R Soc A Math Phys Eng Sci* 455:2861–2877
86. Dorfmann A, Ogden RW (2004) A constitutive model for the Mullins effect with permanent set in particle-reinforced rubber. *Int J Solids Struct* 41:1855–1878
87. Dorfmann A, Pancheri FQ (2012) A constitutive model for the Mullins effect with changes in material symmetry. *Int J Non-Linear Mech* 47:874–887
88. Nguyen VP, Stroeve M, Sluys LJ (2011) Multiscale continuous and discontinuous modelling of heterogeneous materials: a review on recent developments. *J Multiscale Model* 3:229–270
89. Inglis HM, Geubelle PH, Matous K, Tan H, Huang Y (2007) Cohesive modeling of dewetting in particulate composites: micromechanics vs. multiscale finite element analysis. *Mech Mater* 39:580–595
90. Moraleda J, Segurado J, Llorca J (2009) Effect of interface fracture on the tensile deformation of fiber-reinforced elastomers. *Int J Solids Struct* 46:4287–4297
91. Javili A, McBride A, Steinmann P, Reddy B (2014b) A unified computational framework for bulk and surface elasticity theory: a curvilinear-coordinate-based finite element methodology. *Comput Mech* 54:745–762
92. Crisfield MA (1983) An arc-length method including line searches and accelerations. *Int J Numer Methods Eng* 19:1269–1289
93. Fafard M, Massicotte B (1991) Geometrical interpretation of the arc-length method. *Comput Struct* 46:603–615
94. Wriggers P (2008) *Nonlinear finite elements methods*. Springer, Berlin
95. Javili A, Saeb S, Steinmann P (2016) Aspects of implementing constant traction boundary conditions in computational homogenization via semi-dirichlet boundary conditions. *Comput Mech* 59:1–15
96. Firooz S, Saeb S, Chatzigeorgiou G, Meraghni F, Steinmann P, Javili A (2019) Systematic study of homogenization and the utility of circular simplified representative volume element. *Math Mech Solids*. <https://doi.org/10.1177/1081286518823834>
97. Javili A, McBride A, Steinmann P, Reddy B (2012) Relationships between the admissible range of surface material parameters and stability of linearly elastic bodies. *Philos Mag* 92(28–30):3540–3563
98. Nakamura Y, Yamaguchi M, Okubo M, Matsumoto T (1992) Effect of particle size on the fracture toughness of epoxy resin filled with spherical silica. *Polymer* 33:3415–3426
99. Rae PJ, Goldrein HT, Palmer SJP, Field JE, Lewis AL (2002) Quasi-static studies of the deformation and failure of β -HMX based polymer bonded explosives. *Proc R Soc Lond A* 458:743–762
100. Allan Zhong X, Knaus WG (2000) Mechanics of composite materials and structures. *Mech Compos Mater Struct* 7:35–53

Publisher's Note Springer Nature remains neutral with regard to jurisdictional claims in published maps and institutional affiliations.